

A Spectral Confounder Adjustment for Spatial Regression with Multiple Exposures and Outcomes

Shih-Ni Prim^{1,2}, Yawen Guan³, Shu Yang¹, Ana G Rappold⁴, K. Lloyd Hill⁵,
Wei-Lun Tsai⁴, Corinna Keeler⁴, and Brian J Reich¹

¹*Department of Statistics, North Carolina State University, Raleigh, NC, USA*

²*Oak Ridge Institute for Science and Education Fellow at United States Environmental Protection Agency, Center for Public Health and Environmental Assessment, Chapel Hill, NC, USA*

³*Department of Statistics, Colorado State University, Fort Collins, CO, USA*

⁴*United States Environmental Protection Agency, Center for Public Health and Environmental Assessment, Chapel Hill, NC, USA*

⁵*Oak Ridge Associated Universities at United States Environmental Protection Agency, Center for Public Health and Environmental Assessment, Chapel Hill, NC, USA*

June 12, 2025

Abstract

Unmeasured spatial confounding complicates exposure effect estimation in environmental health studies. This problem is exacerbated in studies with multiple health outcomes and environmental exposure variables, as the source and magnitude of confounding bias may differ across exposure/outcome pairs. We propose to mitigate the effects of spatial confounding in multivariate studies by projecting to the spectral domain to separate relationships by the spatial scale and assuming that the confounding bias dissipates at more local scales. Under this assumption and some reasonable conditions, the random effect is uncorrelated with the exposures in local scales, ensuring causal interpretation of the regression coefficients. Our model for the exposure effects is a three-way tensor over exposure, outcome, and spatial scale. We use a canonical polyadic decomposition and shrinkage priors to encourage sparsity and borrow strength across the dimensions of the tensor. We demonstrate the performance of our method in an extensive simulation study and data analysis to understand the relationship between disaster resilience and the incidence of chronic diseases.

Key words: Spatial confounding; causal inference; exposure mixtures; unmeasured confounder; tensor decomposition.

1 Introduction

Commonly occurring in environmental and epidemiological studies, spatial confounding can arise from the presence of spatially-structured missing confounders, which leads to correlated residuals and bias in regression coefficient estimates. Reich et al. (2006) demonstrate that the estimated regression coefficients can be different from models that include or exclude spatial random effects, invalidating inference. To remedy this problem, many explore ways to reduce bias (Paciorek, 2010; Hughes and Haran, 2012; Page et al., 2017; Dupont et al., 2022; Marques et al., 2022; Guan et al., 2023; Adin et al., 2023; Dupont et al., 2024; Khan and Calder, 2022). Geospatial structural equation modeling (gSEM), for example, removes an estimated spatial trend from both the exposure and outcome variables and estimates the parameters using the residuals from the previous step (Thaden and Kneib, 2018; Wiecha and Reich, 2024). On the other hand, when dealing with observational data, causal inference utilizing the potential outcomes framework requires additional assumptions to ensure identifiability. One of such assumptions is that the model includes all confounders, an unverifiable and easily violated assumption (Miao et al., 2023; Wang and Blei, 2019; Reich et al., 2021). To solve the two issues, spatial confounding and violation of the no-unmeasured-confounder assumption, together, one can use the spatial structure to create an estimand that is then removed from the treatment variable to achieve unbiased estimation in the presence of unmeasured spatial confounding (Gilbert et al., 2024; Schnell and Papadogeorgou, 2020; Wiecha and Reich, 2024). Utilizing neighborhood adjustments, we use spectral methods and relax the no-unmeasured-confounder assumption to allow for global-scale confounding, which, as demonstrated in Guan et al. (2023), implies that confounding dissipates in large eigenvalues of the precision matrix in the Conditional Autoregressive (CAR) model.

In addition to the presence of unmeasured confounders, mixtures as exposures present unique problems. Methods were developed in response to the Powering Research through Innovative methods for Mixtures in Epidemiology (PRIME) initiated by National Institute of Environmental Health Sciences (NIEHS) in 2017 (Joubert et al., 2022). Facing challenges such as high dimensionality, collinearity, and interaction between mixtures (Wei et al., 2020; Ferrari and Dunson, 2020; Kowal et al., 2021; Chen et al., 2022), mixture models seek efficient ways to select vari-

able, reduce dimension, and model interaction, utilizing tools such as factor analysis for increasing interpretability and reducing dimension (Reich et al., 2020; Gibson et al., 2021; Roy et al., 2021); Bayesian kernel machine regression for modeling high-dimensional mixtures with interaction (Bobb et al., 2015; Devick et al., 2022); weighted quantile sum (WQS) for variable selection through estimating the weights of each component’s quantile score (Carrico et al., 2015; Gennings et al., 2022); and quantile g-computation, a generalization to WQS (Keil et al., 2020). As many mixture studies are concerned with epidemiological and environmental problems, the causal inference framework has also been utilized (Zigler, 2021; Gennings et al., 2022; Devick et al., 2022).

Among the methods for spatial confounding, few studies include multiple treatments and multiple responses. Note that the terms “treatment” and “exposure” are used interchangeably, as different studies choose different words, but they play the same role in the models. For non-spatial approaches, Zheng et al. (2023) work with one treatment and Kang et al. (2023) deal with multiple treatments; both rely on factor models and use sensitivity analysis to bound the causal effects of unmeasured confounder for multiple outcomes. Miao et al. (2023) use auxiliary variables—which are not causally associated with the response—and null treatments to find causal effects from multiple treatments when unmeasured confounders exist. For spatial data, Marques et al. (2022) investigate a single covariate and multiple covariates in their use of Gaussian random field to reduce spatial confounding. Urdangarin et al. (2024) extend the work of Dupont et al. (2022), who regress the covariates on the thin plate model, and the resulting residuals are used as the covariates while a penalty term for smoothness is included. Urdangarin et al. (2024) find the spectral decomposition of the spatial precision matrix and express the covariate as linear combinations of eigenvectors corresponding to the eigenvalues that are assumed to be confounded. They implemented this simplified model in a multivariate case to jointly analyze the effect of sex ratio on two forms of crimes against women in Uttar Pradesh, India.

We developed a method for modeling causal effects for spatial data with multiple exposures and outcomes in the presence of unmeasured, global spatial confounders. Motivated by Guan et al. (2023), we project spatial data onto the spectral domain, using eigendecomposition of the precision matrix from the CAR model; thus, the observations are transformed into independent vari-

ables, each of which represents a different spatial scale. We relax the no-unmeasured-confounder assumption to allow for global confounding. Under this assumption of local unconfoundedness, the spatial confounder is uncorrelated with the exposures in local scales, ensuring the causal interpretation of the treatment effect. By no means trivial, the extension from univariate to multivariate requires a three-way array to store the multiscale coefficients. The tensor structure captures complicated dependence with constraints on diminishing correlations in local scales. We use canonical polyadic (CP) decomposition to model the tensor coefficients and use shrinkage priors to encourage sparsity and borrow strength from different tensor dimensions (Kolda and Bader, 2009; Guhaniyogi et al., 2017). Though both univariate and multivariate analyses reduce mean squared error due to confounding under the required assumptions, multivariate analysis leverages the low-rankness of the coefficients and the correlation shared among multiple outcomes, gaining efficiency. An extensive simulation study demonstrates the strengths of our proposed method.

The remainder of the paper proceeds as follows. The motivating data are described in Section 2. Sections 3, 4, and 5 introduce the statistical method, examine characteristic of diminishing correlations in local scales, and demonstrate theoretical properties. The method is evaluated using an extensive simulation study in Section 6 and applied to the motivating data in Section 7. Section 8 provides concluding remarks and discusses limitations. Computation, derivations, and additional results are provided in the supplemental materials.

2 Motivating example

To demonstrate the utility of the proposed novel method to control for spatial confounding, we explore the relationship between a local area’s measure of community resilience and adaptive capacity for disaster preparedness and the incidence of prevalent chronic diseases. Composite indices that identify and map community-level resilience and vulnerability are important tools in preparing for and responding to changing environmental conditions. Indicators of preparedness provide a measure of strength to which factors are predictive of adverse outcomes and which ones are not. Across the United States, these indices provide a single number derived from multiple input variables to describe community-level conditions in various contexts, including environmental quality

(Messer et al., 2014), resilience to natural disasters (Flanagan et al., 2011), and neighborhood deprivation (Messer et al., 2006). Most commonly, these composite indices are constructed based on a number of input indicator variables using principal component analysis or factor models (Greco et al., 2019; Reckien, 2018). One challenge in applying composite indices to public health research is a lack of ability to validate and quantify uncertainty related to the predictive performance of indices; additionally, the relationship between composite indices and public health burden is subject to confounding by unmeasured factors at multiple spatial scales which can impact their predictive performance. Because spatial confounding is difficult to control across all spatial scales and all locations, exploring the relationship between health burden and a composite index of community resilience, such as the CDC Social Vulnerability Index (Flanagan et al., 2011), provides a salient motivating example to demonstrate the value of the proposed methodology.

The data used in the current paper includes health outcomes, composite index exposures, and adjusting covariates. The data for the incidence of five prevalent chronic conditions (hypertension, chronic kidney disease, hyperlipidemia, chronic heart failure, and diabetes) was obtained from the Centers for Medicare and Medicaid Services' Chronic Conditions Warehouse. For each Medicare beneficiary, information about chronic health conditions and their annual ZIP-code of residence were provided. We excluded beneficiaries younger than 65 years, since Medicare is available to early enrollees with additional requirements, including disability, End-Stage Renal Disease (ESRD), or Amyotrophic Lateral Sclerosis (ALS), who account for about 15% of all beneficiaries (Short and Weaver, 2008). Each incident health condition for each unique beneficiary contributed one count to the corresponding ZIP-code. The counts were converted to ZIP code tabulated areas (ZCTAs), and the incident rate was calculated as the percentage of the counts divided by the total beneficiaries in the ZCTA (US Department of Health and Human Services, 2023). We used the mean of the incident rates from 2017, 2018, and 2019, three of the most recent years with available data. Maps of outcomes are provided in supplemental materials F.

Social Vulnerability Index for Disaster Management (SVIDM) was created by Center for Disease Control (Centers for Disease Control and Prevention; Agency for Toxic Substances and Disease Registry; Geospatial Research, Analysis, and Services Program, 2018) with the intent to un-

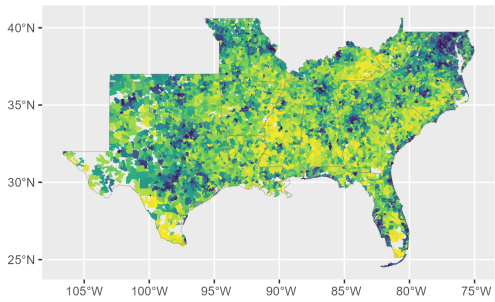
derstand adaptive capacity for natural disasters through the lens of public health. Since our health outcomes came from 2017 to 2019, we used SVI from 2018, created using data from 2014-2018. The data at the ZCTA level was retrieved using the R package `findSVI` (Xu et al., 2025). The index scores range between 0 and 1, with higher scores representing worse abilities to respond to disasters, and are structured in four themes based on 15 factors:

1. Theme 1 describes lack of economic resilience in population based on measures of poverty, unemployment, income, and lack of high school diploma;
2. Theme 2 describes household level adoptive capacity relying on measures of number of people aged 65 or older, aged 17 or younger, number of civilian population with a disability, and number of single-parent households;
3. Theme 3 describes fraction of minority or non-English speaking population;
4. Theme 4 describes the housing type and transportation (multi-unit structures, mobile homes, crowding, no vehicle, group quarters).

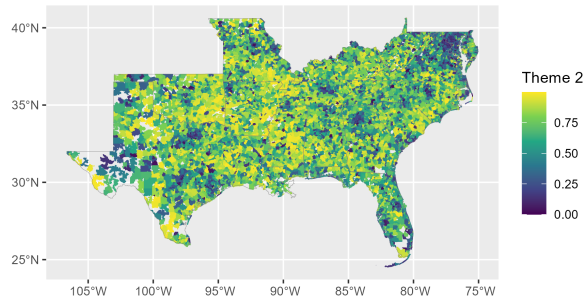
As shown in Figure 1(a)-(d), the first three themes have some degree of spatial pattern, and no global trend is evident for housing type and transportation.

The adjusting covariates include the population size of each ZCTA and whether the ZCTA is considered urban or rural. Population size data was downloaded from the US Census Bureau's 5-year American Community Survey (ACS-5) (US Bureau of the Census, 2023). The logarithmic scale of population is used and shown in Figure 1(f). Urban/rural determination was obtained from 2010 data from Integrated Public Use Microdata Series (IPUMS) National Historical Geographic Information System (NHGIS) (Manson et al., 2024). A ZCTA is considered urban if more than 50% of its population lives in urban areas. The split of rural versus urban areas is almost even: 57.2% urban and 42.8% rural (see Figure 1(e)). We focus on the South region, including seventeen states (Alabama, North Carolina, Oklahoma, Arkansas, Delaware, Florida, Georgia, Kentucky, Louisiana, Maryland, Missouri, Mississippi, South Carolina, Tennessee, Texas, Virginia, West Virginia) and the District of Columbia. After removing ZCTAs with group counts for Medicare data less than 100 and those with health condition incident rates being 0, our dataset contains 10,149 ZCTAs.

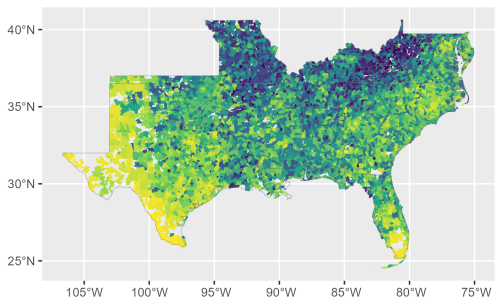
Figure 1: **Maps at ZCTA level for exposures and covariates:** Social Vulnerability Index for Disaster Management themes 1-4 in southern states are in (a)-(d), rural/urban determination in (e), and population size (number of people) in (f).



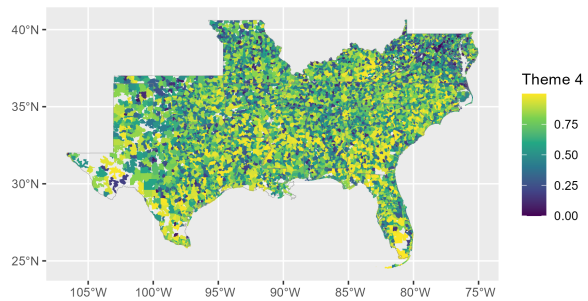
(a) Theme 1



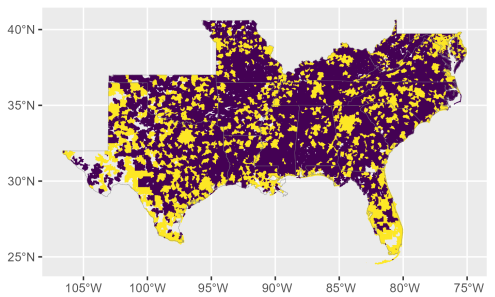
(b) Theme 2



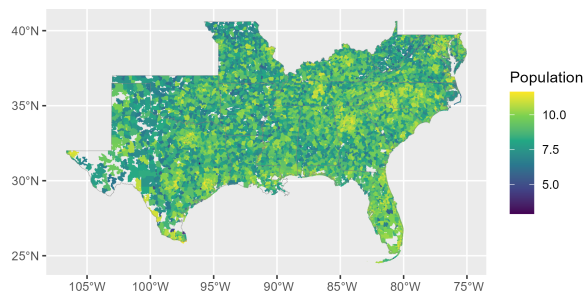
(c) Theme 3



(d) Theme 4



(e) Urbanicity



(f) Population size (log scale)

3 Statistical methods

3.1 Model in the spatial domain

Assume the spatial domain is partitioned into S regions, and $a_{st} = 1$ indicates that regions s and t are adjacent and $a_{st} = 0$ otherwise. The data for region s consists of R response variables, $\{Y_{s1}, \dots, Y_{sR}\}$, E exposure variables, $\{X_{s1}, \dots, X_{sE}\}$ and P known confounding variables, $\{Z_{s1}, \dots, Z_{sP}\}$. In the spatial domain, our model for these data is

$$Y_{sr} = \eta_{0r} + \sum_{p=1}^P Z_{sp}\eta_{pr} + \sum_{e=1}^E X_{se}\beta_{er} + \theta_{sr} + \varepsilon_{sr}, \quad (1)$$

where η_{pr} controls the observed confounder effects, β_{er} are the exposure effects of interests, θ_{sr} are spatially-dependent residuals, and $\varepsilon_{sr} \stackrel{indep}{\sim} \text{Normal}(0, \tau_r^2)$ is error. While the responses are assumed to be normally distributed, the exposures can be all types—continuous, binary, categorical, etc. In the traditional spatial regression model, θ_{sr} is modeled with a spatial process independent of X_{se} . If θ_{sr} is correlated with X_{se} , it is a spatial confounder. If the spatial random effect $\boldsymbol{\theta} = (\theta_{s1}, \dots, \theta_{sR})^\top$ for $s = \{1, \dots, S\}$ is observed, estimation of β_{er} is straightforward. Under the potential outcomes framework and the Stable Unit Treatment Value Assumption (SUTVA), if the potential outcomes follow (1), $(\beta_{1r}, \dots, \beta_{Er})^\top$ represents the average treatment effects of the exposures on outcome r (supplemental materials A). However, when the multivariate, spatial $\boldsymbol{\theta}$ is unobserved and treated as a spatially-correlated error, the dependence between θ_{sr} and X_{se} leads to bias in estimating β_{er} .

Our approach for mitigating this bias makes use of the Conditional Autoregressive (CAR) model. For an arbitrary random vector $\mathbf{V} = (V_1, \dots, V_S)^\top$, the CAR model with Leroux parameterization (Leroux et al., 2000) is multivariate normal with mean zero and covariance matrix $\sigma_V^2 \{(1 - \lambda_V)\mathbf{I}_S + \lambda_V\mathbf{Q}\}^{-1}$ where σ_V^2 controls the variance, $\lambda_V \in (0, 1)$ determines the strength of spatial dependence, and \mathbf{Q} has values $\sum_t a_{st}$ on the diagonal and $-a_{st}$ on the off-diagonals. We denote this model by $\mathbf{V} \sim \text{CAR}(\sigma_V^2, \lambda_V)$.

The multivariate spatial random effects θ_{sr} are modeled using the Linear Model of Coregion-

alization (LMC) (Gelfand et al., 2005; Schmidt and Gelfand, 2003; Wackernagel, 2003; Banerjee et al., 2014; Gelfand and Banerjee, 2010). The LMC assumes the random effects for the R response variables can be explained by $Q \leq R$ latent spatial factors as

$$\theta_{sr} = \sum_{q=1}^Q A_{rq} C_{sq}, \quad (2)$$

where A_{rq} are the factor loadings and $\mathbf{C}_q = (C_{1q}, \dots, C_{Sq})^\top \stackrel{indep}{\sim} \text{CAR}(\sigma_q^2, \lambda_C)$ for $q \in \{1, \dots, Q\}$. This multivariate spatial process includes both spatial dependence via the CAR model and cross dependence via the factor loadings. The cross-correlations have closed forms, i.e., at any location s , two different outcomes have correlation

$$\text{Cor}(\theta_{sr}, \theta_{sr'}) = \frac{\sum_{q=1}^Q \sigma_q^2 A_{rq} A_{r'q}}{\sqrt{\left(\sum_{q=1}^Q \sigma_q^2 A_{rq} A_{rq}\right) \left(\sum_{q=1}^Q \sigma_q^2 A_{r'q} A_{r'q}\right)}}.$$

To ensure identifiability, we set $A_{qq} = 1$ and $A_{rq} = 0$ for $q > r$ (Gelfand and Banerjee, 2010). The remaining terms have prior distributions $A_{rq} \sim \text{Normal}(0, 0.5^2)$, so that the diagonal terms dominate.

While the multivariate CAR model in (2) accounts for multivariate spatial residual dependence, it assumes the random effects θ_{sr} are independent of the exposure variables X_{se} . The spatial model without properly accounting for the dependence between θ and X does not mitigate bias. As a result, the estimates of β_{er} can only be interpreted as causal effects when θ_{sr} and X_{se} are independent, namely, under the assumption of no unmeasured spatial confounder. In Section 3.2 we relax this global assumption.

3.2 Model in the spectral domain

We propose to estimate β_{er} in the spectral domain. By transforming a spatial variable to the spectral domain, we can decompose the spatial information to different scales. The no-unmeasured-confounder assumption requires θ and \mathbf{X} are independent at each scale, where $\mathbf{X} = (\mathbf{X}_1, \dots, \mathbf{X}_E)$,

$\boldsymbol{\theta} = (\boldsymbol{\theta}_1, \dots, \boldsymbol{\theta}_R)$, and \mathbf{X}_e and $\boldsymbol{\theta}_r$ are vectors of length S . We relax this assumption by assuming that global-scale terms are susceptible to confounding whereas local-scale terms are unconfounded, i.e., local unconfoundedness (Guan et al., 2023). Our multiscale estimates can thus capture the true effect at scales where there is assumed to be no confounding.

Our spectral approach uses the graph Fourier transform to decompose the precision matrix into independent signals at different spatial scales. Let $\mathbf{Q} = \mathbf{\Gamma}\mathbf{W}\mathbf{\Gamma}^\top$ be the spectral decomposition of \mathbf{Q} for eigenvector matrix $\mathbf{\Gamma}$ and diagonal matrix \mathbf{W} with diagonal elements equal to the eigenvalues $w_1 \geq \dots \geq w_S$. For arbitrary vector $\mathbf{V} \sim \text{CAR}(\sigma_V^2, \lambda_V)$, premultiplying by the eigenvectors projects the spatial process into the spectral domain. The spectral process is $\mathbf{\Gamma}^\top \mathbf{V} = \mathbf{V}^* = (V_1^*, \dots, V_S^*)^\top$ with

$$V_i^* \stackrel{\text{indep}}{\sim} \text{Normal} \left\{ 0, \sigma_V^2 / (1 - \lambda_V + \lambda_V w_i) \right\}.$$

In the spectral domain, V_i^* are independent across i , allowing us to model each scale separately, account for multiscale confounding, and represent weights of the eigenvectors. Larger weights on the eigenvectors that correspond to small eigenvalues result in smoother spatial process (termed global scale), while larger weights on the eigenvectors corresponding to large eigenvalues lead to rougher spatial process (termed local scale) (Reich et al., 2006).

We specify our model for adjusting for the unmeasured confounders by projecting the model in (1) to the spectral domain. For response $r \in \{1, \dots, R\}$, the data in the spatial domain is $\mathbf{Y}_r = (Y_{1r}, \dots, Y_{Sr})^\top$ and the projection to the spectral domain is $\mathbf{\Gamma}^\top \mathbf{Y}_r = \mathbf{Y}_r^* = (Y_{1r}^*, \dots, Y_{Sr}^*)^\top$, where Y_{ir}^* captures the variation of the outcome r at eigenvalue w_i . Similarly, let Z_{ip}^* , X_{ie}^* and C_{iq}^* for $p \in \{1, \dots, P\}$, $q \in \{1, \dots, Q\}$, and $e \in \{1, \dots, E\}$ be the projected values of the observed confounding, exposure, and spatial variables. Then (1) in the spectral domain is

$$\begin{aligned} Y_{ir}^* &= \eta_{0r} + \sum_{p=1}^P Z_{ip}^* \eta_{pr} + \sum_{e=1}^E X_{ie}^* \beta_{er} + \theta_{ir}^* + \varepsilon_{ir}^*, \text{ where} \\ \theta_{ir}^* &= \sum_{q=1}^Q A_{rq} C_{iq}^* \end{aligned} \quad (3)$$

for $i \in \{1, \dots, S\}$ and $\varepsilon_{ir}^* \stackrel{indep}{\sim} \text{Normal}(0, \tau_r^2)$. In the spectral domain, the latent factors are distributed as $C_{iq}^* \stackrel{indep}{\sim} \text{Normal}\{0, \sigma_q^2 / (1 - \lambda_C + \lambda_C w_i)\}$.

Unlike a standard spatial regression, we model dependence between X_{ie}^* and θ_{ie}^* . We assume a linear confounding relationship between θ_{ir}^* and X_{ie}^* ,

$$\theta_{ir}^* | X_{ie}^* = \alpha_{ier} X_{ie}^* + \xi_{ir},$$

where α_{ier} is the confounding effect of exposure e on response r specific to spatial scale described by eigenvalue w_i . The magnitude of α_{ier} determines the level of correlation between X_{ie}^* and θ_{ir}^* . In this scenario, the scale-invariant true effect β_{er} is generally inseparable from the confounding bias α_{ier} when scales are not explicitly modeled, since increasing X_{ie}^* by one increases the mean response by $\tilde{\beta}_{ier} = \beta_{er} + \alpha_{ier}$.

We use a tensor of dimension $S \times E \times R$ to denote multiscale coefficients $\tilde{\beta}$, which contains $\tilde{\beta}_{ier}$ at scale i , exposure e , and response r . To accurately estimate the coefficient tensor $\tilde{\beta}$, our proposed method allows for a multiscale relationship between \mathbf{X} and $\boldsymbol{\theta}$. A spectral analysis of (3) estimates effects for all S scales. We further assume the strength of correlation diminishes at local scales, i.e. $\alpha_{ier} \downarrow 0$ for large w_i . Thus $\hat{\beta}_{1er}$, the estimate for the multiscale coefficient $\tilde{\beta}_{1er}$, can capture the true β_{er} at eigenvalue w_1 , where the correlation between X_{ie}^* and θ_{ir}^* goes to zero and

$$\tilde{\beta}_{1er} = \beta_{er}.$$

3.3 Bayesian tensor regression

The coefficient $\tilde{\beta}$ includes effects across multiple exposures, multiple responses, and multiple scales and is thus structured as a tensor. While decomposition and the computational aspects have been the focus for tensor research (Zhang and Aeron, 2017; Zhang and Xia, 2018; Zhang and Han, 2019), using tensor for the purpose of statistical inference has seen a recent rise in interest (Mai et al., 2021; Llosa-Vite and Maitra, 2023). We employ Bayesian tensor regression methods for the regression coefficients. Since we envision $\tilde{\beta}_{ier}$ being smooth across scale i but not exposure e or

response r , we represent the variation across i using L spline basis functions B_{i1}, \dots, B_{iL} and

$$\tilde{\beta}_{ier} = \sum_{l=1}^L B_{il} \gamma_{ler},$$

where B_{il} are known B-spline basis functions. The intuition for this model is, first, assuming α_{ier} is a smooth function of w_i , the L spline bases are sufficient to capture its relationship with w_i . Second, the multiple exposures might influence the outcomes through common underlying biological pathways or mechanisms, or the outcomes may respond in similar ways to different exposures. A low-rank model helps identify these latent structures.

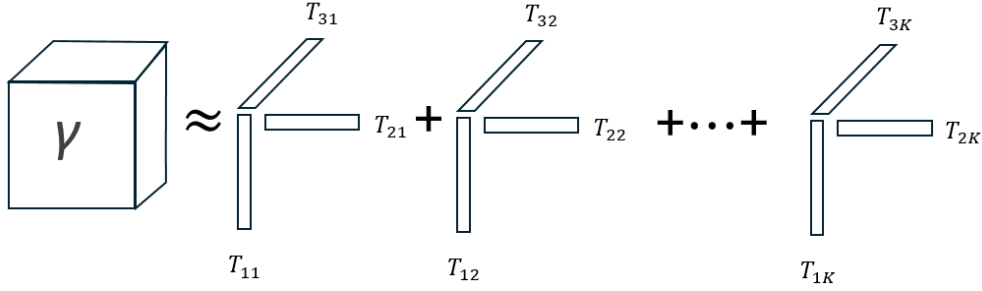
The basis coefficients γ_{ler} are modeled using the Bayesian tensor regression approach in Guhaniyogi et al. (2017). The tensor γ_{ler} is written as a rank K tensor product of factors in each of the three dimensions,

$$\gamma_{ler} = \sum_{k=1}^K T_{1lk} T_{2ek} T_{3rk}. \quad (4)$$

\mathbf{T}_1 , \mathbf{T}_2 , and \mathbf{T}_3 are matrices, whose columns are tensor margins from basis functions, exposures, and outcomes, respectively. More specifically, $\mathbf{T}_t = (T_{t1}, \dots, T_{tK})$, $t = 1, 2, 3$ and tensor margins T_{tk} are defined in Figure 2. Each tensor margin is of the dimension \mathbb{R}^L , \mathbb{R}^E , and \mathbb{R}^R . The latent factors T_{1lk} , T_{2ek} , and T_{3rk} are given Bayesian shrinkage priors to encourage sparsity, assuming a structure of lower than full rank exists (Section 3.4). Using canonical polyadic (CP) tensor decomposition (Kolda and Bader, 2009), the sum of K outer products of the tensor margins approximate the tensor coefficient γ , as represented in Figure 2. The benefits of such decomposition are three-fold. It reduces dimensionality and simplifies the model, representing essential patterns with far fewer parameters and avoiding overfitting. Further, this model captures non-linear relationships and interactions between frequency, exposures, and outcomes. Lastly, the low-rank model makes the results more interpretable and generalizable.

Kolda and Bader (2009) provide a guideline for tensor ranks: $K = \min\{LE, ER, LR\}$. In our simulations, we choose a value smaller than the above value that achieves convergence in MCMC chains. To set a range for L , we consider the relationship between the total number of parameters

Figure 2: **CP decomposition:** \mathbf{T}_1 , \mathbf{T}_2 , and \mathbf{T}_3 are matrices, which are formed by columns that are tensor margins: T_{1k}, T_{2k}, T_{3k} for $k \in \{1, \dots, K\}$. Here $T_{1k} = (T_{11k}, \dots, T_{1Lk})^\top$, $T_{2k} = (T_{21k}, \dots, T_{2Ek})^\top$, $T_{3k} = (T_{31k}, \dots, T_{3Rk})^\top$. The outer product of three tensor margins, each of which a vector of lengths L , E , and R , respectively, is a $L \times E \times R$ tensor. The sum of K such tensors approximates the tensor γ .



in the tensor, $K(L + E + R)$, and the number of response variables SR ,

$$0 < L \leq \frac{SR}{K} - E - R. \quad (5)$$

We fit the model with several L and check trace plots and estimates to choose the optimal L . Supplemental materials E shows the result of sensitivity tests with combinations of different values of L and K .

3.4 Shrinkage priors for tensor coefficients

The tensor regression coefficients in (4) are given horseshoe priors to shrink the regression estimates towards zero for unnecessary ranks or null exposures and outcomes. The horseshoe prior is

$$T_{1lk} \sim N(0, \lambda_{1k}); T_{2ek} \sim N(0, \lambda_{2e}); T_{3rk} \sim N(0, \tau^2 \lambda_{3r} \tau_r^2),$$

where λ_{1k} , λ_{2e} , and λ_{3r} are the variances and control local shrinkage. A global shrinkage hyperparameter, τ , is embedded in T_{3rk} to shrink the coefficients in all outcomes. The variance component τ_r^2 is the variance of the random errors from ε_{ir}^* in (3) and does not affect shrinkage. Following Makalic and Schmidt (2016), we parameterize the shrinkage priors hierarchically. Each shrinkage parameter follows an inverse gamma prior, e.g. $\lambda_{jk} | \nu_j \sim \text{InvGamma}(\frac{1}{2}, \frac{1}{\nu_j})$ for $j \in \{1, 2, 3\}$. Each

hyper-parameter $\nu_j \sim \text{InvGamma}(\frac{1}{2}, 1)$, resulting in the standard half-Cauchy distribution for the square roots of the shrinkage parameters.

4 Understanding confounding in special cases

Our multiscale spectral method for identifying the exposure effects relies on the local unconfoundedness assumption that $\alpha_{ier} \rightarrow 0$ as $w_i \rightarrow \infty$. In this section, we give two special cases to relate this assumption in the spectral domain to more intuitive properties of a spatial model: we first show the connection between w_i and spatial scale through an example of a ring graph (Section 4.1) and then derive and examine α_{ier} for a model with an explicit generative model for the missing spatial confounders (Section 4.2).

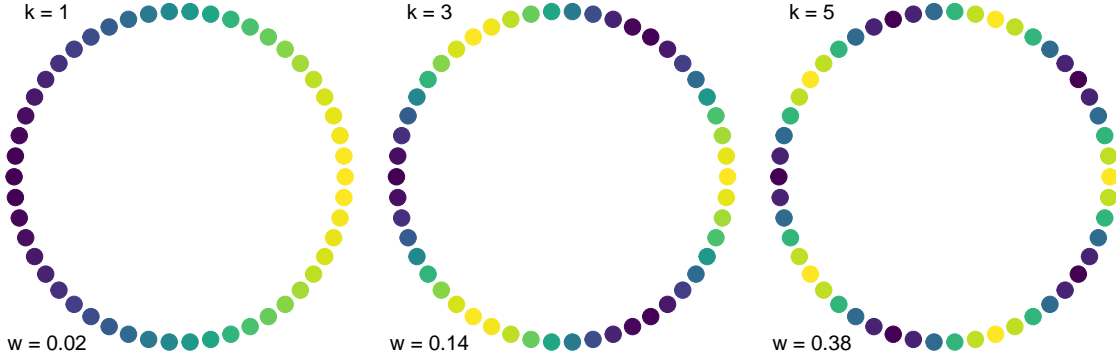
4.1 Connecting eigenvalues and scales in the case of the ring graph

For regions on a regular grid, the eigenvalues and eigenvectors of the adjacency matrix have explicit forms, which lays bare the relationship between the eigenvalues and the spatial scale (van den Heuvel and Pejić, 2001). The simplest case is the ring graph with S vertices $s \in \{1, \dots, S\}$ (Figure 3). The first $S/2$ eigenvectors and eigenvalues are (Rabikka et al., 2022)

$$\Gamma_{is} = \cos(2\pi k_i s/S) \quad \text{and} \quad w_i = 2 - 2 \cos(2\pi k_i/S) \quad (6)$$

for frequency $k_i = i/2, i = 1, \dots, S$ (the remaining $S/2$ eigenpairs have the same form but with a period shift). The data in the spectral domain is $Y_i^* = \sum_{s=1}^S \Gamma_{is} Y_s$, so the eigenvector on the left of Figure 3 with the smallest eigenvalue is effectively the east/west gradient, which we refer to as a global trend. In contrast, the eigenvalue on the right has the largest eigenvalue and corresponds to an average of local differences. Although the connections are not always explicit, we refer to eigenvalues by their scale and in particular focus on the case where $w_i \rightarrow \infty$ and the corresponding eigenvectors measure increasingly local differences.

Figure 3: **Spatial scale and eigenvalues:** Plots of the eigenvectors (Γ) for three frequencies (k) and eigenvalues (w) for the ring graph with $S = 50$ nodes.



4.2 Confounding in a linear, multivariate Gaussian model

In this example, we examine the confounding that arises from a particular model with unmeasured confounding variables to gain insights about the settings that lead to the local unconfoundedness assumption being satisfied. In this particular model, confounding results from n_u latent factors (with unit variance for identifiability) $\mathbf{U}_1, \dots, \mathbf{U}_{n_u} \stackrel{iid}{\sim} \text{CAR}(1, \lambda_U)$ and the exposure and spatial random effects are generated similarly with $\mathbf{M}_{11}, \dots, \mathbf{M}_{1E} \stackrel{iid}{\sim} \text{CAR}(1, \lambda_X)$ and $\mathbf{M}_{21}, \dots, \mathbf{M}_{2R} \sim \text{CAR}(1, \lambda_\theta)$. Let $\mathbf{U} = (\mathbf{U}_1, \dots, \mathbf{U}_{n_u})$, $\mathbf{M}_1 = (\mathbf{M}_{11}, \dots, \mathbf{M}_{1E})$ and $\mathbf{M}_2 = (\mathbf{M}_{21}, \dots, \mathbf{M}_{2R})$. The data are then $\mathbf{X} = \mathbf{U}\mathbf{B}_1 + \mathbf{M}_1\mathbf{S}_1^{1/2}$, $\boldsymbol{\theta} = \mathbf{U}\mathbf{B}_2 + \mathbf{M}_2\mathbf{S}_2^{1/2}$ and $\mathbf{Y} = \mathbf{X}\boldsymbol{\beta} + \boldsymbol{\theta} + \boldsymbol{\epsilon}$, where \mathbf{B}_1 and \mathbf{B}_2 control the strength of confounding, \mathbf{S}_1 and \mathbf{S}_2 are the covariance of the exposures and responses, and $\boldsymbol{\beta}$ is the true effect matrix of interest.

It can be shown (supplemental materials C.3) that the matrix of bias parameters α_{ier} is

$$\alpha_i = \mathbf{B}_2^\top \mathbf{B}_1 \left(\mathbf{B}_1^\top \mathbf{B}_1 + \frac{1 - \lambda_U + \lambda_U w_i}{1 - \lambda_X + \lambda_X w_i} \mathbf{S}_1 \right)^{-1}. \quad (7)$$

If \mathbf{B}_1 or \mathbf{B}_2 is zero, then $\alpha_i = 0$ since $\boldsymbol{\theta}$ and \mathbf{X} are independent and there is no confounding. If $\mathbf{B}_2^\top \mathbf{B}_1 \neq 0$ and there is confounding, then $\alpha_i \rightarrow 0$ as $w_i \rightarrow \infty$ if and only if $\lambda_U > \lambda_X$. That is, the local confounding assumption is satisfied if the missing confounders have stronger spatial dependence than the covariates, which agrees with Paciorek (2010) and others.

5 Identifiability

5.1 Tensor coefficients γ

Regarding tensor coefficients, when α_i goes towards zero, the multiscale regression coefficients $\tilde{\beta} = \gamma \times_n \mathbf{B}$ is identifiable, where \times_n denotes n-mode product (Kolda and Bader, 2009) and \mathbf{B} is of dimension $S \times L$ and contains L B-spline basis functions evaluated at knots. Since \mathbf{B} is given, γ is identifiable, but the individual tensor margins, as discussed in Section 3.3, are not identifiable. As stated in Guhaniyogi et al. (2017), identifiability of tensor margins (columns in T_1, T_2, T_3 , see (4)) comes with three restrictions: (1) scale indeterminacy, (2) permutation indeterminacy, and (3) orthogonal transformation indeterminacy. They found that the non-identifiability of tensor margins does not affect convergence of the tensor coefficients in their simulation studies, and thus imposing identifiability restrictions on tensor margins is unnecessary.

5.2 Other parameters

The distribution of our transformed data for response r is

$$\mathbf{Y}_r^* | \mathbf{X}^* \stackrel{ind}{\sim} N\left(\mathbf{X}^* (\mathbf{1}_S \beta_r + \alpha_r), \tau_r^2 \mathbf{I}_S\right), \quad (8)$$

where $\mathbf{Y}_r^* = (\mathbf{Y}_r^*(w_1), \dots, \mathbf{Y}_r^*(w_S))^\top$, $\alpha_r = (\alpha_r(w_1), \dots, \alpha_r(w_S))^\top$, $\beta_r = (\beta_{1r}, \dots, \beta_{Er})$, $\mathbf{1}_S$ is a length S vector of 1, and \mathbf{X}^* defined as in Section 4. The parameters of interest are $\Theta = (\beta_r, \tau_r^2, \alpha_r)$. To show that the parameters are identifiable, we need to show that $P_1(\mathbf{Y}_r^* | \Theta^{(1)}) = P_2(\mathbf{Y}_r^* | \Theta^{(2)})$ if and only if $\Theta^{(1)} = \Theta^{(2)}$, where $P(\mathbf{Y}_r^* | \Theta)$ is the likelihood function of (8). Thus,

$$\begin{aligned} & (2\pi\tau_r^{2(1)})^{-S/2} \exp \left\{ \left(\mathbf{Y}_r^* - \mathbf{X}^* (\mathbf{1}_S \beta_r^{(1)} + \alpha_r^{(1)}) \right)^\top \left(\mathbf{Y}_r^* - \mathbf{X}^* (\mathbf{1}_S \beta_r^{(1)} + \alpha_r^{(1)}) \right) \right\} \\ &= (2\pi\tau_r^{2(2)})^{-S/2} \exp \left\{ \left(\mathbf{Y}_r^* - \mathbf{X}^* (\mathbf{1}_S \beta_r^{(2)} + \alpha_r^{(2)}) \right)^\top \left(\mathbf{Y}_r^* - \mathbf{X}^* (\mathbf{1}_S \beta_r^{(2)} + \alpha_r^{(2)}) \right) \right\} \\ &\Leftrightarrow \tau_r^{2(1)} = \tau_r^{2(2)} \text{ and } (\mathbf{1}_S \beta_r^{(1)} + \alpha_r^{(1)}) = (\mathbf{1}_S \beta_r^{(2)} + \alpha_r^{(2)}). \end{aligned}$$

When $\alpha_r \rightarrow 0$ in local scales, as described in Section 4, $\beta_r^{(1)} = \beta_r^{(2)}$. Since $\beta + \alpha_i = \tilde{\beta}_i$, $\tilde{\beta}_i$ is identifiable as shown in Section 5.1. The other direction is straightforward. When $\beta_r^{(1)} = \beta_r^{(2)}$ and $\tau_r^{2(1)} = \tau_r^{2(2)}$, $P_1(\mathbf{Y}_r^*|\Theta^{(1)}) = P_2(\mathbf{Y}_r^*|\Theta^{(2)})$ as long as $\alpha_r \rightarrow 0$ for large eigenvalues.

6 Simulation study

We apply the methods described in Section 3 to simulated data to examine how our method performs with different strengths or patterns of spatial confounding. We used four data generation settings as described in Section 6.1. For each setting, we generated $N = 100$ datasets and compared the performance across five models listed in Section 6.2. Computation details are provided in supplemental materials B. This simulation study does not include observed covariates, as the focus here is to demonstrate the effectiveness of our models in adjusting for unmeasured confounding and reducing bias in regression coefficient estimates for the exposures.

6.1 Data generation

We generated data in S spatial locations arranged in a $\sqrt{S} \times \sqrt{S}$ square grid. The response matrix \mathbf{Y} is generated from fixed covariates \mathbf{X} and random effects θ :

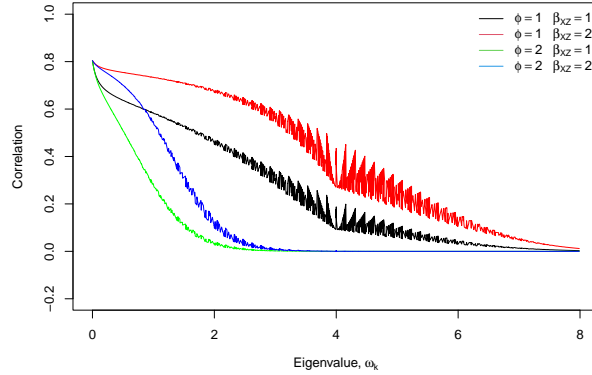
$$\mathbf{Y} = \mathbf{X}\beta + \theta + \epsilon, \text{ where } \epsilon_{sr} \stackrel{iid}{\sim} \text{N}(0, \tau_r^2) \text{ for } s = 1, \dots, S \text{ and } r = 1, \dots, R. \quad (9)$$

Confounding is induced by n_u common factors $\mathbf{U} = \beta_{XZ}\mathbf{G}\mathbf{V}$ where β_{XZ} controls the overall confounding, $\mathbf{V} \sim \text{CAR}(\sigma_V^2, \lambda_V)$, and smoothing controlled by the kernel matrix \mathbf{G} with $G_{ij} = g_{ij}/(\sum_{l=1}^S g_{il})$, $\log(g_{ij}) = -(\|s_i - s_j\|/\phi)^2$, and $s_i \in \{1, \dots, S\}$ is the location of the i^{th} grid cell (Guan et al., 2023). The bandwidth ϕ controls the amount of smoothing, with larger ϕ giving smoother \mathbf{U} .

Given \mathbf{U} , \mathbf{X} and θ are generated with independent components $\mathbf{M}_1\mathbf{S}_1^{1/2}$ and $\mathbf{M}_2\mathbf{S}_2^{1/2}$.

$$\mathbf{X}|\mathbf{U} = \mathbf{U}\mathbf{B}_1 + \mathbf{M}_1\mathbf{S}_1^{1/2}, \text{ where } \mathbf{M}_{1e} \sim \text{CAR}(\sigma_X^2, \lambda_X) \text{ for } e \in \{1, \dots, E\} \text{ and } \mathbf{S}_{1,ij} = \rho_1^{|i-j|} \quad (10)$$

Figure 4: **Correlation versus eigenvalue:** Correlation between X and θ decreases with the increase of eigenvalues. The rate of decrease varies with parameters of extra smoothing ϕ and β_{XZ} , with ϕ controlling the rate of changes in confounding and β_{XZ} controlling overall level of confounding.



and

$$\theta|\mathbf{U} = \mathbf{U}\mathbf{B}_2 + \mathbf{M}_2\mathbf{S}_2^{1/2}, \text{ where } \mathbf{M}_{2r} \sim \text{CAR}(\sigma_\theta^2, \lambda_\theta) \text{ for } r \in \{1, \dots, R\} \text{ and } \mathbf{S}_{2,ij} = \rho_2^{|i-j|}, \quad (11)$$

where both \mathbf{B}_1 (dimension $n_u \times E$) and \mathbf{B}_2 (dimension $n_u \times R$) are non-negative and determine the latent structure between exposure and response. Emulating the relationships commonly found in mixtures and correlated health outcomes, \mathbf{S}_1 (dimension $E \times E$) and \mathbf{S}_2 (dimension $R \times R$) generate correlation among exposures and responses, respectively.

The four data-generation settings use the combinations of the two hyperparameters $(\phi, \beta_{XZ}) = (1, 1), (1, 2), (2, 1), (2, 2)$ for settings 1-4, respectively. As demonstrated in Figure 4, when $\phi = 2$, confounding is strong only for low eigenvalues; when $\phi = 1$, confounding remains strong for all but the highest eigenvalues. Also shown in Figure 4 is how quickly the correlation between X_{ie} and θ_{ir} decreases as the eigenvalue w_i increases to the maximum value in a fixed grid. As the grid becomes finer, the bias lessens. The correlation decreases much faster when $\phi = 2$ compared to $\phi = 1$. The difference affects model performance and demonstrates that our model produces the smallest mean squared error in regression coefficient estimates in the presence of unmeasured spatial confounding.

All scenarios set $\lambda_U = 0.9999, \lambda_X = \lambda_\theta = 0.9, \rho_1 = \rho_2 = 0.9, S = 400, E = 9, R = 5, n_u = 10$. The variances are set at $\sigma_X^2 = 3, \sigma_\theta^2 = 2, \sigma_U^2 = 16$ for \mathbf{U} , and $\tau_r^2 = 4$ for all responses. Values in \mathbf{B}_1 and \mathbf{B}_2 are generated from uniform distribution between 0 and 1. All settings use the same set of coefficients, β . Out of the 10 coefficients (for nine exposures and an intercept), five are non-zero and five are zero. Note that β , though full-rank, has an inherently low-rank structure. Two of the five singular values (1.86, 0.49, 0.12, 0.04, 0.02) are much greater than the rest, accounting for 92.67% of variation.

$$\beta = \begin{bmatrix} 0.3 & 0.4 & 0.2 & 0.1 & 0.5 & 0 & 0 & 0 & 0 & 0 \\ -0.3 & -0.2 & -0.3 & -0.4 & 0.1 & 0 & 0 & 0 & 0 & 0 \\ 0.2 & 0.4 & 0.3 & 0.2 & 0.3 & 0 & 0 & 0 & 0 & 0 \\ 0.3 & 0.5 & 0.4 & 0.3 & 0.4 & 0 & 0 & 0 & 0 & 0 \\ 0.5 & 0.7 & 0.6 & 0.4 & 0.6 & 0 & 0 & 0 & 0 & 0 \end{bmatrix}^\top .$$

6.2 Competing methods and metrics

6.2.1 Competing methods

The first method is our Multivariate Spectral Model (“MSM”) with horseshoe prior for the tensor margin. Method 2 is a univariate version of MSM with each response analyzed separately and is labelled “USM.” The MSM and USM models both set $L = 10$ and $K = 5$; sensitivity to these values is examined in supplemental materials E. Method 3 is the constant coefficient version of our model, with $\tilde{\beta}_i \equiv \beta$ for all i , incapable of accounting for different levels of spatial confounding at different scales and labeled the “naive” method. Methods 4 and 5 adapt the simplified spatial+ method by Urdangarin et al. (2024), who essentially fit (3) using a subset of the data that corresponds to local scales (supplemental materials C.2). We follow Urdangarin et al.’s recommendation and keep 80% (“Spatial+80”) and 40% (“Spatial+40”) of the eigenvectors in the spectral domain for analysis.

6.2.2 Metrics

For the MSM and USM models, we use posterior mean $\hat{\beta}_{1er}$ as the estimate of β_{er} . We evaluate model performance by four metrics: mean squared error (MSE), mean absolute bias (MAB), coverage of 95% intervals, and mean posterior standard deviation (SD). Each metric is averaged over exposure and response. For example,

$$\text{MSE} = \frac{1}{ERN} \sum_{e=1}^E \sum_{r=1}^R \sum_{n=1}^N (\hat{\beta}_{1er}^{(n)} - \beta_{er})^2.$$

For MAB, we calculate the mean absolute bias by taking the absolute values of the mean bias across replicates and then average over exposures and outcomes:

$$\text{MAB} = \frac{1}{ERN} \sum_{e=1}^E \sum_{r=1}^R \left| \sum_{n=1}^N \hat{\beta}_{1er}^{(n)} - \beta_{er} \right|.$$

6.3 Results

A summary of performance metrics is provided in Figure 5. MSM typically has the lowest MSE. Note that MSM has lower MSE compared to USM due to its use of a tensor structure that borrows strength across outcomes. In terms of MAB, MSM is still better than USM and the naive method. The low MAB and high MSE of Spatial+80 and Spatial+40 are noteworthy. The high MSE can be attributed to biases of the methods; since the biases differ among different exposure/outcome pairs, the overall much smaller credible intervals lower MAB. This phenomenon can be verified by the coverage rates around or lower than the nominal rates of Spatial+80 and Spatial+40. In terms of coverage rates, spectral models have nominal or higher coverage rates, suggesting some efficiency loss from using a fraction of the decomposed information. This loss is perhaps unavoidable, since MSM assumes that the most local scale provides the most unbiased estimates. If the assumption is that a range of local scales is unconfounded, some efficiency loss can be avoided, but this is beyond the scope of the current study. Lastly, MSM's standard deviations are higher than the naive method and Spatial+80 but much lower than that of the univariate spectral model, indicating improved efficiency achieved by the multivariate structure through information sharing among outcomes.

Notably, the naive model has especially low 95% coverage rate and high MAB for Setting 2, in which the correlation between \mathbf{X} and θ decreases at the slowest rate (Figure 4). This setting accentuates the importance of considering how confounding varies by scale and adjusting the range of scales on which the estimates should be based. The naive model does not discard information from any scales and thus has detrimental performance for settings where confounding decreases slowly. The correlation drops off at a fastest rate for Setting 3; therefore, the naive model performs better in this setting than in the other three settings. A similar pattern can be observed for Spatial+80 and, to a lesser degree, Spatial+40, again emphasizing the need to match confounding patterns to a model’s adjustment for confounding. Supplemental materials D gives the results separately for true coefficients that are zero and non-zero and the corresponding standard errors.

In summary, if the spatial confounding is known to be present and the goal is inference for causal effects, the multivariate spectral model has competitive MSE, low MAB, and reliable coverage rates. Further, if the effects are inherently low-ranked, the multivariate model has greater efficiency compared to univariate models.

7 Data analysis

After the model selection process, as described in supplemental materials G, we ran the final model with $K = 10$, $L = 10$ on the full dataset with 100,000 iterations, 10,000 burn-ins, and a thinning rate of 10. To highlight the difference between our proposed multiscale method and methods that either lack spatial information or do not allow effects to vary by scale, we compare the results with those from a spatial model (the “naive” model in Section 6) and a non-spatial models (ordinary least square, “OLS”). First and foremost, the data analysis results offer insight into the relationship between disaster resilience and health outcomes. Recall that the exposures are indices between 0 and 1 (higher scores mean less capable to respond to disasters), and the outcomes are incident rates in logarithmic scales. Thus, an increase in the effect estimate linearly increases the predicted log-scaled outcome. To convert the effect estimates to the natural scale, the effect estimate has to be exponentiated. Positive estimates suggest that greater gaps of disaster resilience are associated with increased incidence of chronic diseases and vice versa.

Figure 5: **Simulation results:** MSM is our multivariate spectral model, USM is the univariate spectral model, and the naive model does not allow coefficients to vary by scales. Based on Urdangarin et al. (2024), Spatial+ models retain 80% and 40% of the eigenvectors for Spatial+80 and Spatial+40, respectively. Settings 1-4 set the hyperparameters in the data-generation process (ϕ, β_{XZ}) to be $(1, 1)$, $(1, 2)$, $(2, 1)$, $(2, 2)$, respectively.

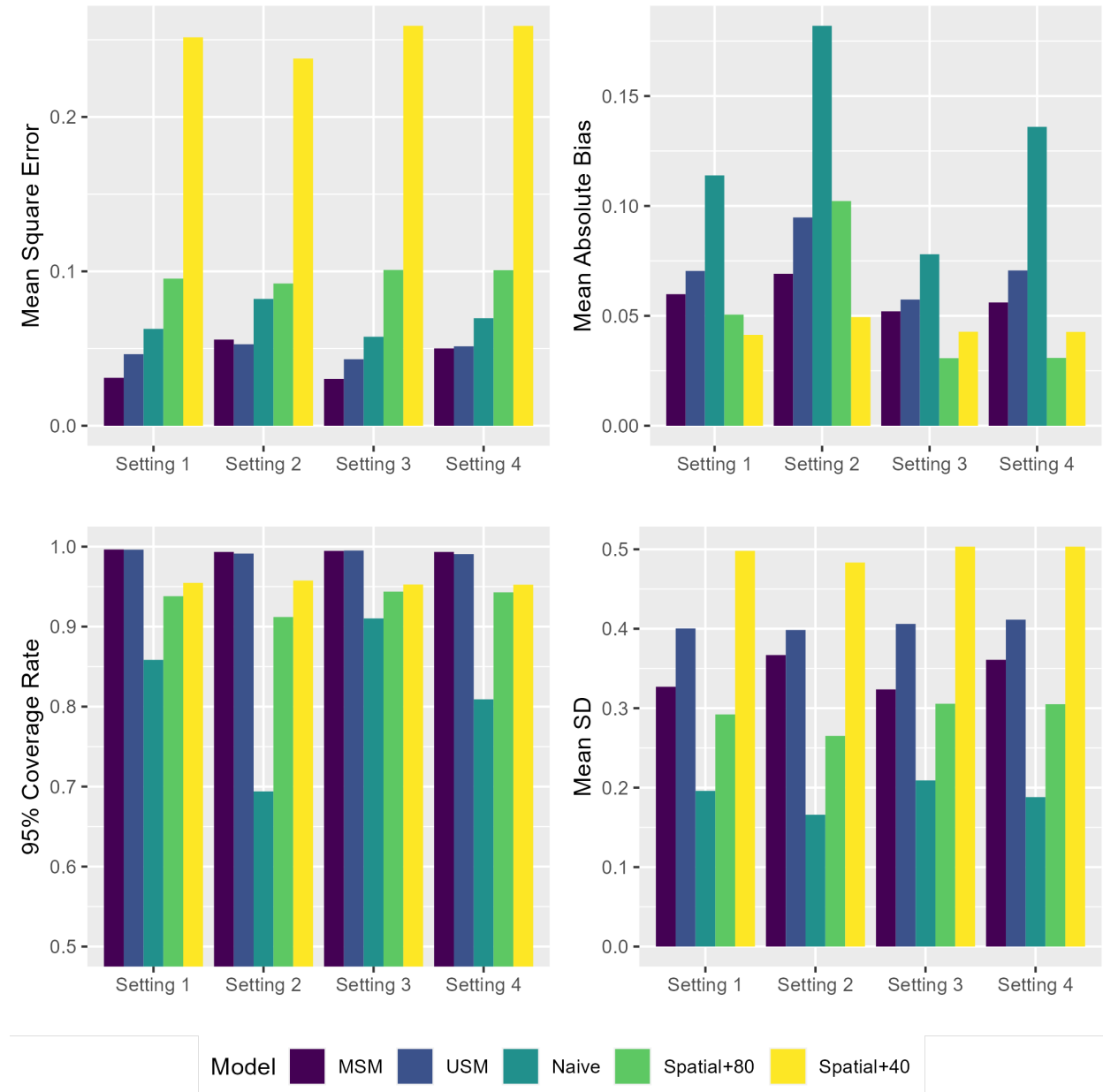


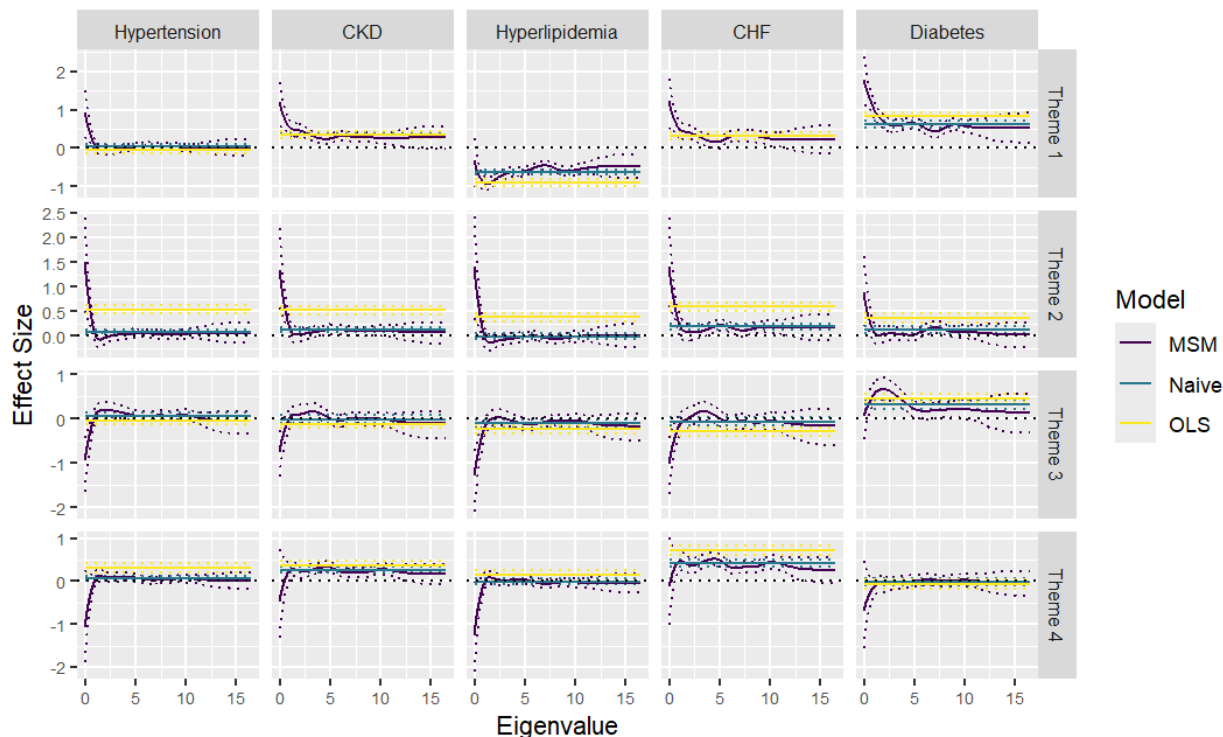
Table 1 shows the percentages of posterior draws of the coefficient estimates greater than 0 for the most local spatial scale. The closer to 0 or 1 the percentages, the stronger evidence there exists for negative or positive associations, respectively, for the exposure-outcome pair. For example, higher scores (less resilience) for theme 1 (lack of economic resilience) are associated with higher incident rates of chronic kidney disease, chronic heart failure, and diabetes but lower rates of diabetes. Although higher scores for Theme 3 tend to be associated with lower incident rates of all conditions except for diabetes, the evidence is not strong enough such that the 95% credible intervals exclude zero. If we use 95% credible intervals as the threshold, as customarily done, the data suggest: 1) higher Theme 1 scores (lack of economic resilience) are correlated with higher incident rates of chronic kidney disease, 2) higher Theme 1 scores are correlated with lower incident rates of hyperlipidemia, 3) higher Theme 1 scores are correlated with higher incident rates of diabetes, and 4) higher Theme 4 scores (housing type and transportation) are correlated with higher incident rates of chronic heart failure. With confounders removed by the design of MSM, these conclusions are less prone to false positives.

Table 1: Percentages of posterior estimates being greater than zero: Positive coefficients suggest that higher scores are associated with worse health outcomes, and negative coefficients suggest otherwise. Percentages over 0.95 (in red) and under 0.05 (in blue) suggest strong evidence for positive or negative associations.

	Hypertension	CKD	Hyperlipidemia	CHF	Diabetes
Theme 1	0.63	0.97	0.00	0.90	1.00
Theme 2	0.73	0.76	0.54	0.90	0.61
Theme 3	0.34	0.26	0.11	0.23	0.77
Theme 4	0.56	0.92	0.35	0.96	0.36

Besides direct understanding about the data, the data analysis results shed light on how MSM can help us rethink spatial statistical analyses. Figure 6 shows how the coefficient estimates vary by spatial scale. The global spatial scale estimates (corresponding to small eigenvalues) are quite different from local scale estimates (corresponding to large eigenvalues). The discrepancy can be quantified by the probabilities of posterior means of the lowest frequency greater than those of the highest frequency. As shown in Table 2, most of the exposure/outcome pairs have very different estimates at the two ends, suggesting the existence of spatial confounding. Housing type and

Figure 6: **Posterior estimates by spatial scale:** The posterior means for each frequency and also the 95% credible intervals are shown below. Larger eigenvalues correspond to local scales, and smaller eigenvalues global scales. The four themes for the disaster resilience index are economic resilience, household level adoptive capacity, fraction of minority, and housing type and transportation. Higher scores indicate less resilience. For chronic conditions, CKD stands for chronic kidney disease, and CHF stands for chronic heart failure. Effect estimates from the naive model and OLS are influenced by information from all scales. Multiscale coefficients from MSM allows for finding unbiased estimates at unconfounded spatial scales.



transportation theme, as shown in Figure 1, stands out for the lack of global trends. Corresponding to this observation, Table 2 shows that, for Theme 4, the coefficient estimates from the most local and most global scales have the largest percentages of overlap (except for hyperlipidemia), indicating a lesser degree of spatial confounding. A spectral method like MSM can help identify spatial confounding and caution against using ordinary spatial or non-spatial methods.

Also shown in Figure 6 is how the global spatial scales can nudge the estimates towards biased for the naive model and OLS. Although MSM and naive models' credible intervals generally overlap, the naive model takes in all information and its credible intervals might be overly narrow,

Table 2: **Probabilities of coefficient estimates at the lowest frequency greater than those at the highest frequency:** Values close to one (in red) or zero (in blue) mean that coefficient estimates vary by spatial scales, which means spatial confounding is highly likely. As shown below, strong spatial confounding is suspected for most exposure/outcome pairs.

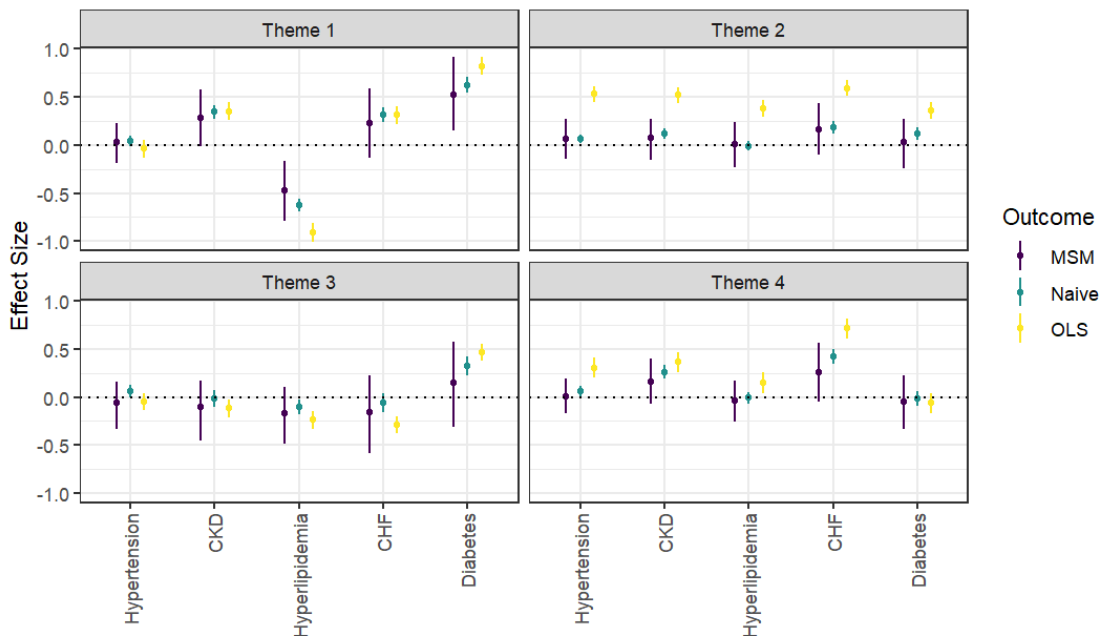
	Hypertension	CKD	Hyperlipidemia	CHF	Diabetes
Theme 1	1.00	1.00	0.68	1.00	1.00
Theme 2	1.00	1.00	1.00	1.00	0.99
Theme 3	0.00	0.00	0.00	0.00	0.39
Theme 4	0.08	0.12	0.01	0.22	0.13

resulting in false positive results. As shown in Figure 5, the naive model has the lowest mean standard deviation but the coverage rate can be lower than nominal levels, especially when spatial confounding is strong. Similarly, OLS takes in information from all locations but, unlike the naive model, does not consider spatial locations. Its results also have smaller uncertainty and can be influenced by spatial confounding to a larger degree, particularly evident in plots for household composition and disability. To account for spatial relationships in OLS models, we also tried including information such as state. But this crude approach neither considers the neighboring relationship between ZCTAs nor properly adjusts for confounding.

The multiscale coefficients also highlight how units of areas could affect the result. As explained in Section 4.1, derived from the eigendecomposition of the adjacency matrix’s precision matrix, eigenvalues correspond to spatial scales: the larger the eigenvalues, the more local the scales. Eigenvalues cannot be uniquely translated into specific physical distances; however, among the pairwise distances of ZCTAs, the 10th percentile is around 283 kilometers, and the 90th percentile is around 1638 kilometers. For context, the mean width of a state is around 400 kilometers. These numbers and the curves in Figure 6 reveal that very different conclusions can be drawn, depending on whether data come from the census tract, ZCTA, county, state, or region level. If a method like the naive model is used, even though the spatial relationships between location are considered, since the information comes from all levels of averaging, confounding is hard to avoid.

A forest plot in Figure 7 shows the coefficient estimates with 95% credible intervals for MSM, naive model, and OLS. This is essentially the same as Figure 6, except the curves are sliced at the largest eigenvalues. As discussed above, MSM has the largest uncertainty because it breaks down

Figure 7: **Forest plot for estimated coefficients:** MSM is our multivariate spectral model. The naive model is spatial but does not allow coefficients to vary by scales. The OLS model is non-spatial and treats each location independently. MSM has the largest uncertainty but provides unbiased estimates, assuming the most local spatial scale is unconfounded.



the estimates by spatial scales and its estimates come from the most local spatial scale. Further, the estimates from the three models show how adjusting for spatial relationships (going from OLS to naive) and separating signals by spatial scales (going from naive to MSM) can prevent false positive results. The coefficient estimates from the naive model are generally closer to null, suggesting that including spatial information can account for some confounding. The naive model, nonetheless, can still be over-confident, as shown in Figure 5.

Lastly, the tensor estimates provide information about the latent structure of the health effects. To provide a succinct representation of this structure, we use the R package `rTensor` (Li et al., 2018) to find a rank-2 canonical polyadic tensor decomposition of the posterior mean of the tensor $\hat{\gamma}$ in (4). Each curve in Figure 8 represents a tensor margin (see Figure 2). For basis functions, term with index near one capture global features and indices near $L = 10$ capture local features. For tensor margins representing basis functions, the first factor (green) captures global trends. For tensor margins representing exposures, the first factor is positive for Theme 1 (lack of economic

resilience) and Theme 2 (household level adoptive capacity) and negative for Theme 3 (fraction of minority) and Theme 4 (housing type and transportation). This explains the differences between global- and local-scale effect estimates in Figure 6. Factor 2 (purple) dominates for the local-scale trends of interest and Theme 1 has the highest loading and thus the strongest effects in Figure 7. For this factor and thus the final estimates in Figure 7, the responses have similar loadings except for hyperlipidemia, which is also reflected in Figure 7. The tensor margins for outcomes indicate that the exposure effects for chronic kidney disease and chronic heart failure are largely similar, while the effects for other outcomes differ. The complexity in data with multiple exposures and multiple outcomes makes it difficult to parse complex structure. By using a tensor structure, MSM offers a way to construct interpretable latent structures, enabling understanding of the relationship among different dimensions.

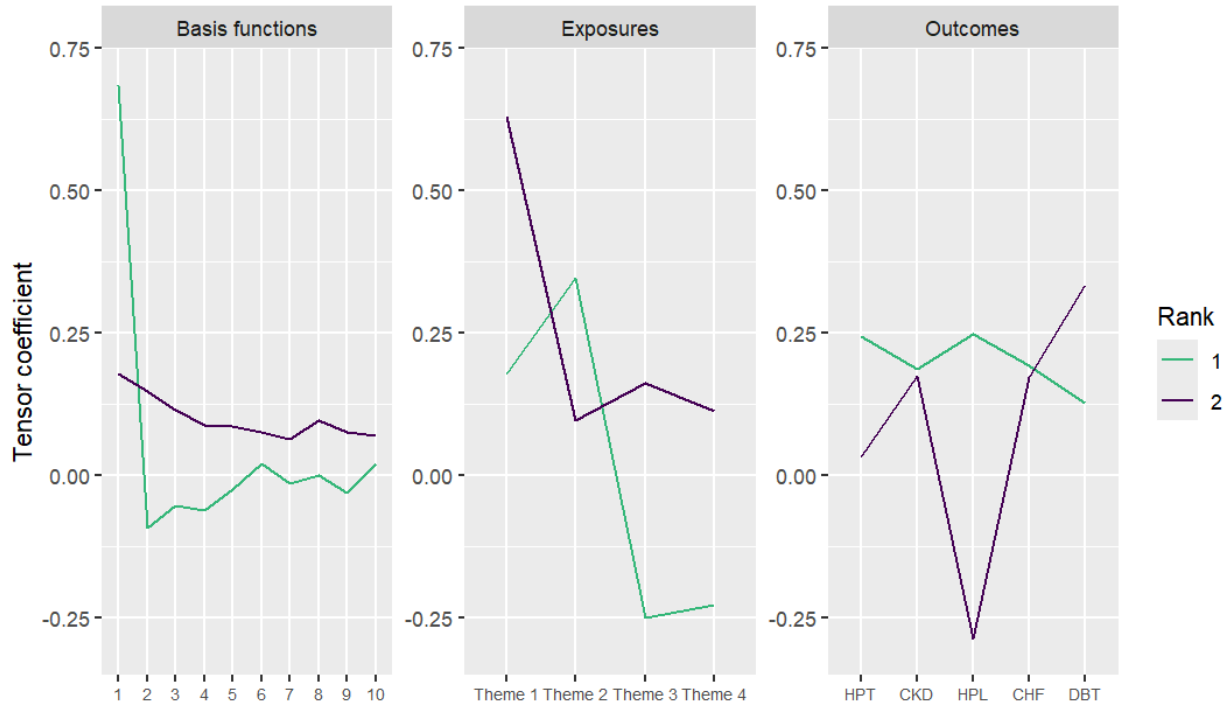
8 Discussion

We introduce a multivariate spectral model (MSM) for areal data that estimates effects of multiple exposures on multiple outcomes in the presence of spatial confounding. The model relaxes the no-unmeasured-confounder assumption and permits global confounding. As the simulation study demonstrates, when the conditions hold, the MSM method has low MSE and reliable empirical coverage. Nonetheless, being a parametric model, the proposed MSM has its limitations in the pre-specified model. A semiparametric or nonparametric framework could provide more flexibility and robustness in the case that the model is misspecified. Further, unmeasured local confounding is unverifiable. We leave these limitations for future research.

Data analysis shows the associations between disaster resilience index in four themes and the incidence of five chronic diseases. The 95% credible intervals show that ZCTA areas lacking economic resilience (high scores for Theme 1) are more likely to have higher incident rates of chronic kidney disease and diabetes but lower rates of hyperlipidemia, while lacking disaster resilience in terms of housing type and transportation (high scores for Theme 4) are associated with higher incident rates of chronic heart failure.

Besides being able to estimate effects with adjustment for unmeasured spatial confounders,

Figure 8: **Tensor estimates:** The curves show one rank-2 CP decomposition of the posterior means of the low-rank tensor that is of the dimension $L \times E \times R$, as presented in (4). For basis functions, the x-axis shows the ten basis functions that represent weights from the most global (1) to the most local (10). The x-axis for exposures includes the four themes of the disaster resilience index: lack of economic resilience, household level adoptive capacity, fraction of minority, and housing type and transportation; and that for outcomes contains the five health conditions: hypertension, chronic kidney disease, hyperlipidemia, chronic heart failure, and diabetes. Each curve represents a tensor margin and shows the relationship among basis functions, exposures, and outcomes.



MSM offers a more nuanced way to understand spatial data, as demonstrated in Section 7, and encourages the consideration of how the units of data and the latent structures can play a role in the effect estimates. MSM can be used, combined with domain knowledge and understanding of real-world data, to detect spatial confounding, determine the range of spatial scales from which unbiased coefficient estimates can be obtained, and take the posterior draws from the specified range as the best answer to the problem at hand.

Acknowledgements

Research reported in this publication was supported by the National Heart, Lung, And Blood Institute of the National Institutes of Health under Award Number T32HL079896, National Institutes of Health grant R01ES031651-01, and National Science Foundation grant DMS2152887. The content is solely the responsibility of the authors and does not necessarily represent the official views of the National Institutes of Health.

This project was supported by an appointment (of S.E.C.) to the Research Participation Program at the Center for Public Health and Environmental Assessment, U.S. Environmental Protection Agency (EPA), administered by the Oak Ridge Institute for Science and Education through an interagency agreement between the U.S. Department of Energy and the U.S. EPA.

Disclaimer

Although this work has been reviewed for publication by the U.S. EPA, it does not necessarily reflect the views and policies of the agency. Mention of trade names or commercial products does not constitute endorsement or recommendation for use.

References

- Adin, A., Goicoa, T., Hodges, J. S., Schnell, P. M. and Ugarte, M. D. (2023) Alleviating confounding in spatio-temporal areal models with an application on crimes against women in India. *Statistical Modelling*, **23**, 9–30.
- Banerjee, S., Carlin, B. P. and Gelfand, A. E. (2014) *Hierarchical Modeling and Analysis for Spatial Data*. CRC Press.
- Bobb, J. F., Valeri, L., Claus Henn, B., Christiani, D. C., Wright, R. O., Mazumdar, M., Godleski, J. J. and Coull, B. A. (2015) Bayesian kernel machine regression for estimating the health effects of multi-pollutant mixtures. *Biostatistics*, **16**, 493–508.
- Carrico, C., Gennings, C., Wheeler, D. C. and Factor-Litvak, P. (2015) Characterization of weighted quantile sum regression for highly correlated data in a risk analysis setting. *Journal of Agricultural, Biological, and Environmental Statistics*, **20**, 100–120.

- Centers for Disease Control and Prevention; Agency for Toxic Substances and Disease Registry; Geospatial Research, Analysis, and Services Program (2018) CDC/ATSDR Social Vulnerability Index 2018 Database U.S. https://www.atsdr.cdc.gov/placeandhealth/svi/data_documentation_download.html.
- Chen, H. Y., Li, H., Argos, M., Persky, V. W. and Turyk, M. E. (2022) Statistical methods for assessing the explained variation of a health outcome by a mixture of exposures. *International Journal of Environmental Research and Public Health*, **19**, 2693.
- Devick, K. L., Bobb, J. F., Mazumdar, M., Claus Henn, B., Bellinger, D. C., Christiani, D. C., Wright, R. O., Williams, P. L., Coull, B. A. and Valeri, L. (2022) Bayesian kernel machine regression-causal mediation analysis. *Statistics in Medicine*, **41**, 860–876.
- Dupont, E., Marques, I. and Kneib, T. (2024) Demystifying Spatial Confounding. *arXiv:2309.16861*.
- Dupont, E., Wood, S. N. and Augustin, N. H. (2022) Spatial+: A novel approach to spatial confounding. *Biometrics*, **78**, 1279–1290.
- Ferrari, F. and Dunson, D. B. (2020) Identifying main effects and interactions among exposures using Gaussian processes. *The Annals of Applied Statistics*, **14**, 1743–1758.
- Flanagan, B. E., Gregory, E. W., Hallisey, E. J., Heitgerd, J. L. and Lewis, B. (2011) A Social Vulnerability Index for Disaster Management. *Journal of homeland security and emergency management*, **8**.
- Gelfand, A. and Banerjee, S. (2010) Multivariate Spatial Process Models. In *Handbook of Spatial Statistics* (eds. A. Gelfand, P. Diggle, M. Fuentes and P. Guttorp), 495–515. CRC Press.
- Gelfand, A. E., Banerjee, S. and Gamerman, D. (2005) Spatial process modelling for univariate and multivariate dynamic spatial data. *Environmetrics*, **16**, 465–479.
- Gennings, C., Svensson, K., Wolk, A., Lindh, C., Kiviranta, H. and Bornehag, C.-G. (2022) Using metrics of a mixture effect and nutrition from an observational study for consideration towards causal inference. *International Journal of Environmental Research and Public Health*, **19**, 2273.
- Gibson, E. A., Rowland, S. T., Goldsmith, J., Paisley, J., Herbstman, J. B. and Kiourmourtzoglou, M.-A. (2021) Bayesian non-parametric non-negative matrix factorization for pattern identification in environmental mixtures. *arXiv:2109.12164*.
- Gilbert, B., Datta, A., Casey, J. A. and Ogburn, E. L. (2024) A causal inference framework for spatial confounding. *arXiv:2112.14946*.
- Greco, S., Ishizaka, A., Tasiou, M. and Torrìsi, G. (2019) On the Methodological Framework of Composite Indices: A Review of the Issues of Weighting, Aggregation, and Robustness. *Social Indicators Research*, **141**, 61–94.

- Guan, Y., Page, G. L., Reich, B. J., Ventrucci, M. and Yang, S. (2023) Spectral adjustment for spatial confounding. *Biometrika*, **110**, 699–719.
- Guhaniyogi, R., Qamar, S. and Dunson, D. B. (2017) Bayesian tensor regression. *The Journal of Machine Learning Research*, **18**, 2733–2763.
- van den Heuvel, J. and Pejić, S. (2001) Using Laplacian Eigenvalues and Eigenvectors in the Analysis of Frequency Assignment Problems. *Annals of Operations Research*, **107**, 349–368.
- Hughes, J. and Haran, M. (2012) Dimension reduction and alleviation of confounding for spatial generalized linear mixed models. *Journal of the Royal Statistical Society Series B: Statistical Methodology*, **75**, 139–159.
- Joubert, B. R., Kioumourtzoglou, M.-A., Chamberlain, T., Chen, H. Y., Gennings, C., Turyk, M. E., Miranda, M. L., Webster, T. F., Ensor, K. B., Dunson, D. B. and Coull, B. A. (2022) Powering research through innovative methods for mixtures in epidemiology (PRIME) program: novel and expanded statistical methods. *International Journal of Environmental Research and Public Health*, **19**, 1378.
- Kang, S., Franks, A. and Antonelli, J. (2023) Sensitivity analysis with multiple treatments and multiple outcomes with applications to air pollution mixtures. *arXiv:2311.12252*.
- Keil, A. P., Buckley, J. P., O’Brien, K. M., Ferguson, K. K., Zhao, S. and White, A. J. (2020) A Quantile-Based g-Computation Approach to Addressing the Effects of Exposure Mixtures. *Environmental Health Perspectives*, **128**, 47004.
- Khan, K. and Calder, C. A. (2022) Restricted Spatial Regression Methods: Implications for Inference. *Journal of the American Statistical Association*, **117**, 482–494.
- Kolda, T. G. and Bader, B. W. (2009) Tensor Decompositions and Applications. *SIAM Review*, **51**, 455–500.
- Kowal, D. R., Bravo, M., Leong, H., Bui, A., Griffin, R. J., Ensor, K. B. and Miranda, M. L. (2021) Bayesian variable selection for understanding mixtures in environmental exposures. *Statistics in Medicine*, **40**, 4850–4871.
- Leroux, B. G., Lei, X. and Breslow, N. (2000) Estimation of Disease Rates in Small Areas: A new Mixed Model for Spatial Dependence. In *Statistical Models in Epidemiology, the Environment, and Clinical Trials* (eds. M. E. Halloran and D. Berry), 179–191. New York, NY: Springer New York.
- Li, J., Bien, J. and Wells, M. T. (2018) rTensor: An R package for multidimensional array (tensor) unfolding, multiplication, and decomposition. *Journal of Statistical Software*, **87**, 1–31.
- Llosa-Vite, C. and Maitra, R. (2023) Reduced-Rank Tensor-on-Tensor Regression and Tensor-Variate Analysis of Variance. *IEEE Transactions on Pattern Analysis and Machine Intelligence*, **45**, 2282–2296.

- Mai, Q., Zhang, X., Pan, Y. and Deng, K. (2021) A Doubly Enhanced EM Algorithm for Model-Based Tensor Clustering. *Journal of the American Statistical Association*, **117**, 2120–2134.
- Makalic, E. and Schmidt, D. F. (2016) A Simple Sampler for the Horseshoe Estimator. *IEEE Signal Processing Letters*, **23**, 179–182.
- Manson, S., Schroeder, J., Riper, D. V., Knowles, K., Kugler, T., Roberts, F. and Ruggles, S. (2024) IPUMS National Historical Geographic Information System: Version 19.0 [dataset]. Minneapolis, MN: IPUMS.
- Marques, I., Kneib, T. and Klein, N. (2022) Mitigating spatial confounding by explicitly correlating Gaussian random fields. *Environmetrics*, **33**, e2727.
- Messer, L. C., Jagai, J. S., Rappazzo, K. M. and Lobdell, D. T. (2014) Construction of an environmental quality index for public health research. *Environmental Health*, **13**.
- Messer, L. C., Laraia, B. A., Kaufman, J. S., Eyster, J., Holzman, C., Culhane, J., Elo, I., Burke, J. G. and O’Campo, P. (2006) The development of a standardized neighborhood deprivation index. *Journal of Urban Health*, **83**, 1041–1062.
- Miao, W., Hu, W., Ogburn, E. L. and Zhou, X.-H. (2023) Identifying Effects of Multiple Treatments in the Presence of Unmeasured Confounding. *Journal of the American Statistical Association*, **118**, 1953–1967.
- Paciorek, C. J. (2010) The Importance of Scale for Spatial-Confounding Bias and Precision of Spatial Regression Estimators. *Statistical Science*, **25**, 107–125.
- Page, G. L., Liu, Y., He, Z. and Sun, D. (2017) Estimation and Prediction in the Presence of Spatial Confounding for Spatial Linear Models. *Scandinavian Journal of Statistics*, **44**, 780–797.
- Rabikka, V., Asir, T. and Prathibha, M. E. (2022) Spectrum of Graphs over Rings: A Survey. In *Algebra and Related Topics with Applications* (eds. M. Ashraf, A. Ali and V. De Filippis), 427–449. Singapore: Springer Nature Singapore.
- Reckien, D. (2018) What is in an index? Construction method, data metric, and weighting scheme determine the outcome of composite social vulnerability indices in New York City. *Regional Environmental Change*, **18**, 1439–1451.
- Reich, B. J., Guan, Y., Fourches, D., Warren, J. L., Sarnat, S. E. and Chang, H. H. (2020) Integrative Statistical Methods for Exposure Mixtures and Health. *The Annals of Applied Statistics*, **14**, 1945–1963.
- Reich, B. J., Hodges, J. S. and Zadnik, V. (2006) Effects of Residual Smoothing on the Posterior of the Fixed Effects in Disease-Mapping Models. *Biometrics*, **62**, 1197–1206.
- Reich, B. J., Yang, S., Guan, Y., Giffin, A. B., Miller, M. J. and Rappold, A. (2021) A Review of Spatial Causal Inference Methods for Environmental and Epidemiological Applications. *International Statistical Review*, **89**, 605–634.

- Roy, A., Lavine, I., Herring, A. H. and Dunson, D. B. (2021) Perturbed factor analysis: Accounting for group differences in exposure profiles. *The Annals of Applied Statistics*, **15**, 1386–1404.
- Rubin, D. B. (1974) Estimating causal effects of treatments in randomized and nonrandomized studies. *Journal of Educational Psychology*, **66**, 688–701.
- (1980) Randomization Analysis of Experimental Data: The Fisher Randomization Test Comment. *Journal of the American Statistical Association*, **75**, 591–593.
- Schmidt, A. M. and Gelfand, A. E. (2003) A Bayesian coregionalization approach for multivariate pollutant data. *Journal of Geophysical Research: Atmospheres*, **108**.
- Schnell, P. and Papadogeorgou, G. (2020) Mitigating Unobserved Spatial Confounding when Estimating the Effect of Supermarket Access on Cardiovascular Disease Deaths. *arXiv:1907.12150*.
- Short, P. F. and Weaver, F. (2008) Transitioning to Medicare before age sixty-five. *Health Affairs*, **27**.
- Thaden, H. and Kneib, T. (2018) Structural Equation Models for Dealing With Spatial Confounding. *The American Statistician*, **72**, 239–252.
- Urdangarin, A., Goicoa, T., Kneib, T. and Ugarte, M. D. (2024) A simplified spatial+ approach to mitigate spatial confounding in multivariate spatial areal models. *Spatial Statistics*, **59**, 100804.
- US Bureau of the Census (2023) American Community Survey 5-Year Data (2009-2021). <https://www.census.gov/data/developers/data-sets/acs-5year.html>.
- US Department of Health and Human Services (2023) Chronic conditions data warehouse. <https://www2.ccwdata.org/web/guest/condition-categories-chronic/>.
- Wackernagel, H. (2003) *Multivariate Geostatistics*. Springer Berlin, Heidelberg.
- Wang, Y. and Blei, D. M. (2019) The Blessings of Multiple Causes. *Journal of the American Statistical Association*, **114**, 1574–1596.
- Wei, R., Reich, B. J., Hoppin, J. A. and Ghosal, S. (2020) Sparse Bayesian additive nonparametric regression with application to health effects of pesticides mixtures. *Statistica Sinica*, **30**, 55–79.
- Wiecha, N. and Reich, B. J. (2024) Two-stage Spatial Regression Models for Spatial Confounding. *arXiv:2404.09358*.
- Xu, H., Li, R. and Bilal, U. (2025) *findSVI: Calculate Social Vulnerability Index for Communities*. R package version 0.2.0.
- Zhang, A. and Han, R. (2019) Optimal Sparse Singular Value Decomposition for High-Dimensional High-Order Data. *Journal of the American Statistical Association*, **114**, 1708–1725.

- Zhang, A. and Xia, D. (2018) Tensor SVD: Statistical and Computational Limits. *IEEE Transactions on Information Theory*, **64**, 7311–7338.
- Zhang, Z. and Aeron, S. (2017) Exact Tensor Completion Using t-SVD. *IEEE Transactions on Signal Processing*, **65**, 1511–1526.
- Zheng, J., Wu, J., D’Amour, A. and Franks, A. (2023) Sensitivity to Unobserved Confounding in Studies with Factor-Structured Outcomes. *Journal of the American Statistical Association*, **119**, 2026–2037.
- Zigler, C. M. (2021) Invited commentary: the promise and pitfalls of causal inference with multivariate environmental exposures. *American Journal of Epidemiology*, **190**, 2658–2661.

A Spectral Confounder Adjustment for Spatial Regression with Multiple Exposures and Outcomes

Supplemental materials

June 12, 2025

A Spatial causal framework

Under the potential outcome framework (Rubin, 1974), we let

$$Y_{ir}(\mathbf{x}_i) = \sum_{e=1}^E \beta_{ier} x_{ie} + \sum_{p=1}^P \alpha_{pr} Z_{ip} + \theta_{ir} + \epsilon_{ir},$$

where $Y_{ir}(\mathbf{x}_i)$ is the potential outcome at location i when the levels of E exposures for the location i are $\mathbf{x}_i = (x_{i1}, \dots, x_{iE})^T$. Z_{ip} is covariate p at location i , α_{pr} is the coefficient of the covariate p associated with the outcome r , θ_{ir} is a confounder for outcome r at location i , and ϵ_{ir} is random noise and distributed by $N(0, \tau_r^2)$.

Since our exposure is continuous, our estimand is $\beta_{er} = E[Y_{ir}(x_{i1}, \dots, x_{ie} + 1, \dots, x_{iE}) - Y_{ir}(x_{i1}, \dots, x_{ie}, \dots, x_{iE})]$, the average treatment effect (ATE) of exposure e on response r . Since we can only observe one outcome at each location, the potential outcome framework requires several assumptions to ensure identifiability. One assumption is the stable unit treatment value assumption (SUTVA), which means only one version for each level of the treatment exists and the potential outcome of one unit is not affected by that of another unit (Rubin, 1980). In the spatial context, the second half of SUTVA means the effect does not spill over to neighboring areas. Further, the assumption of consistency states that the observed outcome is the same as the potential outcome determined by the observed treatment, i.e. $Y_{ir} = Y_{ir}(\mathbf{x}_i)$.

The next assumption, latent ignorability, states that, given the treatment \mathbf{x}_i and the confounder θ_{ir} , the potential outcome $Y_{ir}(\mathbf{x}_i)$ is independent of the treatment variable, i.e., $\mathbf{X} \perp \mathbf{Y}(\mathbf{x}) | \mathbf{Z}, \boldsymbol{\theta}$ for

all $\mathbf{x} \in \text{supp}(\mathbf{X})$, where

$$\begin{aligned}\mathbf{X} &= (\mathbf{x}_1 \cdots \mathbf{x}_S)^\top, & \mathbf{x}_S &= (x_{s1} \cdots x_{sE}) \\ \mathbf{Y} &= (\mathbf{Y}_{i1} \cdots \mathbf{Y}_{iR}), & \mathbf{Y}_{ir} &= (Y_{1r} \cdots Y_{Sr})^\top \\ \boldsymbol{\theta} &= (\boldsymbol{\theta}_1 \cdots \boldsymbol{\theta}_R), & \boldsymbol{\theta}_r &= (\theta_{1r} \cdots \theta_{Sr})^\top\end{aligned}$$

One last crucial assumption is no unmeasured confounders. In Section 3.2 of the main document, we propose a spectral method to account for the unmeasured confounder in the global scale and assumes that no local confounders exist.

B Computational details

The MCMC sampler is comprised of Gibbs and Metropolis-Hasting sampling. For Gibbs sampling, the full-conditional posterior distributions are provided in supplemental materials C.1. For Metropolis-Hasting sampling, our algorithm keeps the acceptance rate around 40%. Each MCMC simulation is run for 5,000 iterations with 1,000 burn-ins. We use different values of L and K and set $L = 10$ and $K = 5$ with verification that the MCMC chains achieve good convergence by examining trace plots and effective sample sizes.

C Derivations

C.1 Full conditional distribution

The likelihood function is

$$Y_{ir}^* \sim N\left(\sum_{e=1}^E X_{ie}^* \left(\sum_{l=1}^L B_{il} \left(\sum_{k=1}^K T_{1lk} T_{2ek} T_{3rk}\right)\right) + \mathbf{A}_r \mathbf{C}_i^{*\top}, \tau_r^2\right).$$

The full conditional distributions are given below.

C.1.1 Update T_{1lk}

The full conditional depends on

$$\begin{aligned}
 L_{lk} &= \sum_{r=1}^R \left(\sum_{i=1}^S \left(\sum_{e=1}^E X_{ie}^* B_{il} T_{2ek} T_{3rk} \right)^2 / \tau_r^2 \right), \\
 A_{lk} &= L_{lk} + \frac{1}{\lambda_{1k}}, \\
 h_{i,k,l,r}^{(l)} &= Y_{ir}^* - \underbrace{\sum_{e=1}^E X_{ie}^* \sum_{z \neq l} B_{iz} T_{1zk} T_{2ek} T_{3rk}}_{\text{same rank, different basis function}} - \underbrace{\sum_{e=1}^E X_{ie}^* \sum_{l=1}^L B_{il} \sum_{j \neq k} T_{1lj} T_{2ej} T_{3rj}}_{\text{different rank, all basis functions}} - \mathbf{A}_r \mathbf{C}_i^{*\top}, \\
 B_{lk} &= \sum_{r=1}^R \left(\sum_{i=1}^S h_{i,k,l,r}^{(l)} \right) / \tau_r^2.
 \end{aligned}$$

Then, $T_{1lk} | \text{rest} \sim N(B_{lk}/A_{lk}, 1/A_{lk})$.

C.1.2 Update T_{2ek}

The full conditional depends on

$$\begin{aligned}
 E_{ek} &= \sum_{r=1}^R \left(\sum_{i=1}^S X_{ie}^* \sum_{l=1}^L B_{il} T_{1lk} T_{3rk} \right)^2 / \tau_r^2, \\
 A_{ek} &= E_{ek} + \frac{1}{\lambda_{2e}}, \\
 h_{i,k,e,r}^{(e)} &= Y_{ir}^* - \underbrace{\sum_{z \neq e} X_{iz}^* \sum_{l=1}^L B_{il} T_{1lk} T_{2zk} T_{3rk}}_{\text{same rank, different exposure}} - \underbrace{\sum_{e=1}^E X_{ie}^* \sum_{l=1}^L B_{il} \sum_{j \neq k} T_{1lj} T_{2ej} T_{3rj}}_{\text{different rank, all exposures}} - \mathbf{A}_r \mathbf{C}_i^{*\top}, \\
 B_{ek} &= \sum_{r=1}^R \left(\sum_{i=1}^S h_{i,k,e,r}^{(e)} \right) / \tau_r^2.
 \end{aligned}$$

Then, $T_{2ek} | \text{rest} \sim N(B_{ek}/A_{ek}, 1/A_{ek})$.

C.1.3 Update T_{3rk}

The full conditional depends on

$$\begin{aligned}
 R_{rk} &= \sum_{i=1}^S \left(\sum_{e=1}^E X_{ie}^* \sum_{l=1}^L B_{il} T_{1lk} T_{2ek} \right)^2 / \tau_r^2, \\
 A_{rk} &= R_{rk} + \frac{1}{\lambda_{3r} \tau^2 \tau_r^2}, \\
 h_{i,k,r}^{(r)} &= Y_{ir}^* - \underbrace{\sum_{e=1}^E X_{ie}^* \sum_{l=1}^L B_{il} \sum_{j \neq k} T_{1lj} T_{2ej} T_{3rj}}_{\text{different rank, same response}} - \mathbf{A}_r \mathbf{C}_i^{*\top}, \\
 B_{rk} &= \left(\sum_{i=1}^S h_{i,k,r}^{(r)} \right) / \tau_r^2.
 \end{aligned}$$

Then, $T_{3rk} | \text{rest} \sim N(B_{rk}/A_{rk}, 1/A_{rk})$.

C.1.4 Update τ_r^2

The prior distribution is $\tau_r^2 \sim \text{InvGamma}(a, b)$. Thus,

$$\tau_r^2 | \text{rest} \sim \text{InvGamma} \left(\frac{S+K}{2} + a, \frac{\sum_{i=1}^S (Y_{ir}^* - \mathbf{X}_i^* \boldsymbol{\beta}_r - \mathbf{A}_r \mathbf{C}_i^{*T})^2}{2} + \frac{\sum_{k=1}^K T_{3rk}^2}{2\lambda_{3r}\tau^2} + b \right).$$

C.1.5 Update σ_q^2

The prior distribution is $\sigma_q^2 \sim \text{InvGamma}(c, d)$. Then,

$$\sigma_q^2 | \text{rest} \sim \text{InvGamma} \left(\frac{S}{2} + c, \sum_{i=1}^S \frac{\mathbf{C}_q^{*2} (1 - \lambda_C + \lambda_C w_i)}{2} + d \right)$$

C.1.6 Update \mathbf{A}_r

The prior distribution is $A_{rq} \sim N(0, 0.5^2)$. Thus,

$$A_{rq} | \text{rest} \sim N \left(\left(\mathbf{C}_q^{*T} \boldsymbol{\Sigma}_r^{-1} \mathbf{C}_q^* + \frac{1}{0.5^2} \right)^{-1} \left(\mathbf{C}_q^{*T} \boldsymbol{\Sigma}_r^{-1} (\mathbf{Y}_r^* - \mathbf{X}^* \boldsymbol{\beta}_r) \right), \left(\mathbf{C}_q^{*T} \boldsymbol{\Sigma}_r^{-1} \mathbf{C}_q^* + \frac{1}{0.5^2} \right)^{-1} \right).$$

We update one row at a time:

$$\mathbf{A}_r | \text{rest} \sim \mathcal{N} \left(\left(\mathbf{C}^{*T} \boldsymbol{\Sigma}_r^{-1} \mathbf{C}^* + \frac{1}{0.5^2} \mathbf{I}_Q \right)^{-1} \left(\mathbf{C}^{*T} \boldsymbol{\Sigma}_r^{-1} (\mathbf{Y}_r^* - \mathbf{X}^* \boldsymbol{\beta}_r) \right), \left(\mathbf{C}^{*T} \boldsymbol{\Sigma}_r^{-1} \mathbf{C}^* + \frac{1}{0.5^2} \mathbf{I}_Q \right)^{-1} \right).$$

Although all columns are used for the full conditionals, we only update the cells corresponding in the lower triangle.

C.1.7 Update \mathbf{C}_q

The prior distribution is $\mathbf{C}_q \sim \text{CAR}(\sigma_q^2, \lambda_U)$. Then,

$$\mathbf{C}_q^{*T} | \text{rest} \sim \mathcal{N} \left\{ \mathbf{D}_{C_q}^{-1} \left(\sum_{r=1}^R A_{rq} \boldsymbol{\Sigma}_r^{-1} \left(\mathbf{Y}_r^* - \mathbf{X}^* \boldsymbol{\beta}_r - \sum_{p \neq q} \mathbf{C}_p^* A_{rp} \right) \right), \mathbf{D}_{C_q}^{-1} \right\},$$

where \mathbf{D}_{C_q} is a $S \times S$ diagonal matrix with the diagonal components $\left(\sum_{r=1}^R \frac{A_{rq}^2}{\tau_r^2} + \frac{1 - \lambda_U + \lambda_U w_i}{\sigma_q^2} \right)$ for $i \in \{1, 2, \dots, S\}$.

C.2 Implementation of Spatial+

In a univariate case, Urdangarin et al. (2024) decompose the covariates \mathbf{X} into two groups of linear combinations of eigenvectors, $\mathbf{X} = \mathbf{F} + \mathbf{F}'$ with $\mathbf{F} = a_1 \mathbf{D}_1 + \dots + a_{n-(k+1)} \mathbf{D}_{n-(k+1)}$ and $\mathbf{F}' = a_{n-k} \mathbf{D}_{n-k} + \dots + a_n \mathbf{D}_n$, where \mathbf{D}_i are eigenvectors and a_i are constants. To connect this model to our implementation, we rewrite \mathbf{F} and \mathbf{F}' : $\mathbf{F} = \boldsymbol{\Gamma}_1 A_1$, $\mathbf{F}' = \boldsymbol{\Gamma}_2 A_2$ where the eigenvector matrix $\boldsymbol{\Gamma} = \begin{bmatrix} \boldsymbol{\Gamma}_1 & \boldsymbol{\Gamma}_2 \end{bmatrix}$, which corresponds to large and small eigenvalues, and A_1 and A_2 contain the coefficients of the corresponding linear combinations. Their model uses $\mathbf{F} = \boldsymbol{\Gamma}_1 A_1$, as the covariates in the spatial domain:

$$\mathbf{X}^* = \boldsymbol{\Gamma}^\top \mathbf{X} = \begin{bmatrix} \boldsymbol{\Gamma}_1^\top \\ \boldsymbol{\Gamma}_2^\top \end{bmatrix} \left(\boldsymbol{\Gamma}_1 A_1 + \boldsymbol{\Gamma}_2 A_2 \right) = \begin{bmatrix} \boldsymbol{\Gamma}_1^\top \boldsymbol{\Gamma}_1 A_1 + \boldsymbol{\Gamma}_1^\top \boldsymbol{\Gamma}_2 A_2 \\ \boldsymbol{\Gamma}_2^\top \boldsymbol{\Gamma}_1 A_1 + \boldsymbol{\Gamma}_2^\top \boldsymbol{\Gamma}_2 A_2 \end{bmatrix} = \begin{bmatrix} A_1 \\ A_2 \end{bmatrix},$$

which is equivalent to the covariates in our spectral model, A_1 .

C.3 Derivations of bias from unmeasured confounding

The matrix \mathbf{U} introduces confounding to \mathbf{X} and $\boldsymbol{\theta}$. The derivation here does not include extra smoothing introduced in Section 6.1 and focuses on demonstrating how correlation, and thus bias, decreases at highest eigenvalues when $\lambda_U > \lambda_X$.

$$\mathbf{U} \sim \text{CAR}(1, \lambda_U)$$

$$\mathbf{X}|\mathbf{U} = \mathbf{U}\mathbf{B}_1 + \mathbf{M}_1\mathbf{S}_1^{1/2}, \text{ where } \mathbf{M}_1 \sim \text{CAR}(1, \lambda_X) \text{ and } \mathbf{S}_{1,ij} = \rho_1^{|i-j|}$$

$$\boldsymbol{\theta}|\mathbf{U} = \mathbf{U}\mathbf{B}_2 + \mathbf{M}_2\mathbf{S}_2^{1/2}, \text{ where } \mathbf{M}_2 \sim \text{CAR}(1, \lambda_\theta) \text{ and } \mathbf{S}_{2,ij} = \rho_2^{|i-j|}.$$

In the spatial domain,

$$\mathbf{Y} = \mathbf{X}\boldsymbol{\beta} + \boldsymbol{\theta} + \boldsymbol{\epsilon}.$$

To project the data into the spectral domain, we pre-multiply \mathbf{Y} , \mathbf{X} , and $\boldsymbol{\theta}$ by the eigenvector matrix Γ .

$$\underbrace{\Gamma^\top \mathbf{Y}}_{\mathbf{Y}^*} = \underbrace{\Gamma^\top \mathbf{X}}_{\mathbf{X}^*} \boldsymbol{\beta} + \underbrace{\Gamma^\top \boldsymbol{\theta}}_{\boldsymbol{\theta}^*} + \underbrace{\Gamma^\top \boldsymbol{\epsilon}}_{\boldsymbol{\epsilon}^*}$$

$$\mathbf{U}_i^* = \Gamma^\top \mathbf{U}_i \sim \text{N}\left(0, \frac{1}{1 - \lambda_U + \lambda_U w_i} \mathbf{I}_{n_u}\right)$$

$$\mathbf{X}_i^* | \mathbf{U}_i^* = \mathbf{U}_i^* \mathbf{B}_1 + \mathbf{M}_{1i}^* \mathbf{S}_1^{1/2}, \text{ where } \mathbf{M}_{1i}^* \mathbf{S}_1^{1/2} \sim \text{N}\left(0, \frac{1}{1 - \lambda_X + \lambda_X w_i} \mathbf{S}_1\right)$$

and

$$\boldsymbol{\theta}_i^* | \mathbf{U}_i^* = \mathbf{U}_i^* \mathbf{B}_2 + \mathbf{M}_{2i}^* \mathbf{S}_2^{1/2}, \text{ where } \mathbf{M}_{2i}^* \mathbf{S}_2^{1/2} \sim \text{N}\left(0, \frac{1}{1 - \lambda_\theta + \lambda_\theta w_i} \mathbf{S}_2\right)$$

Now we can derive expectations and covariances:

$$E(\mathbf{X}_i^* | \mathbf{U}_i^*) = E(\boldsymbol{\theta}_i^* | \mathbf{U}_i^*) = 0 \Rightarrow E(\mathbf{X}_i^*) = E(\boldsymbol{\theta}_i^*) = 0$$

$$\begin{aligned}
Var(\mathbf{X}_i^*) &= E\{Var(\mathbf{X}_i^*|\mathbf{U}_i^*)\} + Var\{E(\mathbf{X}_i^*|\mathbf{U}_i^*)\} \\
&= \frac{1}{1 - \lambda_U + \lambda_U w_i} \mathbf{B}_1^\top \mathbf{B}_1 + \frac{1}{1 - \lambda_X + \lambda_X w_i} \mathbf{S}_1.
\end{aligned}$$

Similarly,

$$\begin{aligned}
Var(\boldsymbol{\theta}_i^*) &= E\{Var(\boldsymbol{\theta}_i^*|\mathbf{U}_i^*)\} + Var\{E(\boldsymbol{\theta}_i^*|\mathbf{U}_i^*)\} \\
&= \frac{1}{1 - \lambda_U + \lambda_U w_i} \mathbf{B}_2^\top \mathbf{B}_2 + \frac{1}{1 - \lambda_\theta + \lambda_\theta w_i} \mathbf{S}_2.
\end{aligned}$$

Then,

$$Cov(\mathbf{X}_i^*, \boldsymbol{\theta}_i^*) = \mathbf{B}_1^\top Cov(\mathbf{U}_i^*) \mathbf{B}_2^\top = \frac{1}{1 - \lambda_U + \lambda_U w_i} \mathbf{B}_1^\top \mathbf{B}_2$$

Thus the joint distribution of $\boldsymbol{\theta}_i^*$ and \mathbf{X}_i^* is:

$$\begin{pmatrix} \boldsymbol{\theta}_i^* \\ \mathbf{X}_i^* \end{pmatrix} \sim \text{MVN} \left(\begin{bmatrix} 0 \\ 0 \end{bmatrix}, \begin{bmatrix} Var(\boldsymbol{\theta}_i^*) & \frac{1}{1 - \lambda_U + \lambda_U w_i} \mathbf{B}_2^\top \mathbf{B}_1 \\ \frac{1}{1 - \lambda_U + \lambda_U w_i} \mathbf{B}_1^\top \mathbf{B}_2 & Var(\mathbf{X}_i^*) \end{bmatrix} \right)$$

Thus, by the property of multivariate normal distribution,

$$\begin{aligned}
E(\boldsymbol{\theta}_i^*|\mathbf{X}_i^*) &= \mathbf{X}_i^* \left(\frac{1}{1 - \lambda_U + \lambda_U w_i} \mathbf{B}_2^\top \mathbf{B}_1 Var(\mathbf{X}_i^*)^{-1} \right) \\
&= \mathbf{X}_i^* \left\{ \frac{1}{1 - \lambda_U + \lambda_U w_i} \mathbf{B}_2^\top \mathbf{B}_1 \left(\frac{1}{1 - \lambda_U + \lambda_U w_i} \mathbf{B}_1^\top \mathbf{B}_1 + \frac{1}{1 - \lambda_X + \lambda_X w_i} \mathbf{S}_1 \right)^{-1} \right\}^\top \\
&= \mathbf{X}_i^* \underbrace{\left\{ \mathbf{B}_2^\top \mathbf{B}_1 \left(\mathbf{B}_1^\top \mathbf{B}_1 + \frac{1 - \lambda_U + \lambda_U w_i}{1 - \lambda_X + \lambda_X w_i} \mathbf{S}_1 \right)^{-1} \right\}^\top}_{=:\boldsymbol{\alpha}_i}.
\end{aligned}$$

The model can be written as $\mathbf{Y}_i^*|\mathbf{X}_i^* = \mathbf{X}_i^*; \boldsymbol{\beta} + \boldsymbol{\theta}_i^*|\mathbf{X}_i^* + \boldsymbol{\epsilon}_i^* = \mathbf{X}_i^* \boldsymbol{\beta} + \mathbf{X}_i^* \boldsymbol{\alpha}_i + \boldsymbol{\epsilon}_i^*$.

D Additional simulation study results

Tables 3 and 4 provides five performance metrics—MSE, MAB, standard deviation, coverage rate for 95% credible interval, and credible interval length—separately for coefficients ($\hat{\boldsymbol{\beta}}$) that are

nonzero and zero.

Similar to the results presented in Section 7, MSM typically has low MSE and MAB. When the results are separated by whether coefficients are zero or nonzero, a slight difference is noted. MSM consistently outperforms other models for zero coefficients. While its MSE and MAB are still low for nonzero coefficients, the strengths are not as apparent across settings. More specifically, MSM's MAB are higher than those of Spatial+40 for nonzero coefficients. While MSM has overall reliable performance, it is especially strong in determining exposures with null effects.

E Sensitivity analysis for varying L and K

Our approach allows for flexibility in two parameters: the number of spline basis functions (L) and the rank of the tensor decomposition (K). Table 5 shows the MSE and coverage rates for several L and K for $N = 20$ replicates from simulation Setting 2. MSE is not sensitive to different L and K , but coverage rates might be too low if K is set too low. Our recommendation is setting L and K to be around and slightly larger than the expected complexity and make sure K is not too small. Setting K to be too large, however, risks poor convergence and slow computation.

F Maps for health conditions

G Model selection

To select the best model, we compare model performance of four combinations of the MSM method: $K = 5, 10$ and $L = 5, 10$. We split the dataset that contains 10,149 ZCTAs into a training set (80%) and a test set (20%) and use log scores as the performance metric. The trained model is used to predict the responses of the test set, and the log scores are the mean of the log likelihood of the observed data, given the predicted mean and standard deviation. All models are run with 20,000 iterations, 2,000 burn-ins, and thinning rate 10. Trace plots confirm convergence for all coefficients. All log scores are shown in Table 6.

Table 3: **Simulation results:** The first two columns indicate the values for hyperparameters for data generation. Results here are separate for nonzero versus zero coefficients. The five models are Multivariate Spectral Model (MSM), Univariate Spectral Model (USM), a model that do not separate estimates by scale (Naive), and Simplified Spatial+ that retains 80% and 40% of the eigenvectors. The numbers in parentheses are standard errors.

(a) Mean Square Error

ϕ	β_{XZ}	coefficients	MSM	USM	Naive	Spatial+80	Spatial+40
1	1	Nonzero	0.05 (0.01)	0.08 (0.01)	0.05 (0.01)	0.08 (0.01)	0.22 (0.03)
1	2	Nonzero	0.06 (0.01)	0.09 (0.01)	0.07 (0.01)	0.08 (0.01)	0.21 (0.03)
2	1	Nonzero	0.05 (0.01)	0.08 (0.01)	0.05 (0.01)	0.09 (0.01)	0.22 (0.03)
2	2	Nonzero	0.07 (0.01)	0.09 (0.01)	0.06 (0.01)	0.09 (0.01)	0.22 (0.03)
1	1	Zero	0.02 (0.00)	0.02 (0.01)	0.07 (0.01)	0.11 (0.01)	0.28 (0.04)
1	2	Zero	0.05 (0.01)	0.03 (0.01)	0.09 (0.01)	0.10 (0.01)	0.26 (0.04)
2	1	Zero	0.02 (0.00)	0.02 (0.01)	0.06 (0.01)	0.11 (0.01)	0.29 (0.04)
2	2	Zero	0.04 (0.01)	0.02 (0.01)	0.08 (0.01)	0.11 (0.01)	0.29 (0.04)

(b) Mean Absolute Bias

ϕ	β_{XZ}	coefficients	MSM	USM	Naive	Spatial+80	Spatial+40
1	1	nonzero	0.10 (0.02)	0.11 (0.02)	0.10 (0.02)	0.04 (0.03)	0.04 (0.04)
1	2	nonzero	0.11 (0.02)	0.14 (0.02)	0.17 (0.02)	0.09 (0.02)	0.05 (0.04)
2	1	nonzero	0.10 (0.02)	0.10 (0.02)	0.07 (0.02)	0.03 (0.03)	0.04 (0.04)
2	2	nonzero	0.10 (0.02)	0.12 (0.02)	0.12 (0.02)	0.03 (0.03)	0.04 (0.04)
1	1	zero	0.03 (0.01)	0.04 (0.01)	0.13 (0.02)	0.06 (0.03)	0.04 (0.05)
1	2	zero	0.04 (0.02)	0.06 (0.01)	0.19 (0.02)	0.12 (0.03)	0.05 (0.05)
2	1	zero	0.02 (0.01)	0.02 (0.01)	0.09 (0.02)	0.03 (0.03)	0.04 (0.05)
2	2	zero	0.02 (0.02)	0.03 (0.01)	0.15 (0.02)	0.03 (0.03)	0.04 (0.05)

(c) Mean Posterior Standard Deviation

ϕ	β_{XZ}	coefficients	MSM	USM	Naive	Spatial+80	Spatial+40
1	1	nonzero	0.35 (0.01)	0.47 (0.02)	0.18 (0.00)	0.26 (0.00)	0.45 (0.00)
1	2	nonzero	0.38 (0.01)	0.46 (0.02)	0.15 (0.00)	0.24 (0.00)	0.43 (0.00)
2	1	nonzero	0.35 (0.01)	0.48 (0.02)	0.19 (0.00)	0.27 (0.00)	0.45 (0.00)
2	2	nonzero	0.37 (0.02)	0.48 (0.02)	0.17 (0.00)	0.27 (0.00)	0.45 (0.00)
1	1	zero	0.31 (0.01)	0.35 (0.02)	0.21 (0.00)	0.31 (0.00)	0.54 (0.00)
1	2	zero	0.36 (0.02)	0.35 (0.02)	0.18 (0.00)	0.28 (0.00)	0.52 (0.00)
2	1	zero	0.31 (0.01)	0.35 (0.02)	0.22 (0.00)	0.33 (0.00)	0.55 (0.00)
2	2	zero	0.35 (0.02)	0.36 (0.02)	0.20 (0.00)	0.33 (0.00)	0.55 (0.00)

Table 4: **Simulation results (continued)**

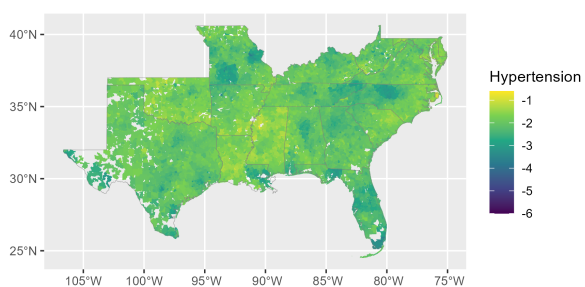
(d) Empirical Coverage

ϕ	β_{XZ}	coefficients	MSM	USM	Naive	Spatial+80	Spatial+40
1	1	nonzero	0.99 (0.01)	0.99 (0.00)	0.85 (0.03)	0.94 (0.02)	0.95 (0.02)
1	2	nonzero	0.98 (0.01)	0.98 (0.01)	0.68 (0.04)	0.92 (0.03)	0.95 (0.02)
2	1	nonzero	0.99 (0.01)	0.99 (0.01)	0.90 (0.03)	0.94 (0.02)	0.95 (0.02)
2	2	nonzero	0.99 (0.01)	0.98 (0.01)	0.80 (0.04)	0.94 (0.02)	0.95 (0.02)
1	1	zero	1.00 (0.00)	1.00 (0.00)	0.86 (0.03)	0.94 (0.02)	0.96 (0.02)
1	2	zero	1.00 (0.00)	1.00 (0.00)	0.71 (0.04)	0.91 (0.03)	0.96 (0.02)
2	1	zero	1.00 (0.00)	1.00 (0.00)	0.92 (0.03)	0.95 (0.02)	0.95 (0.02)
2	2	zero	1.00 (0.00)	1.00 (0.00)	0.81 (0.03)	0.94 (0.02)	0.95 (0.02)

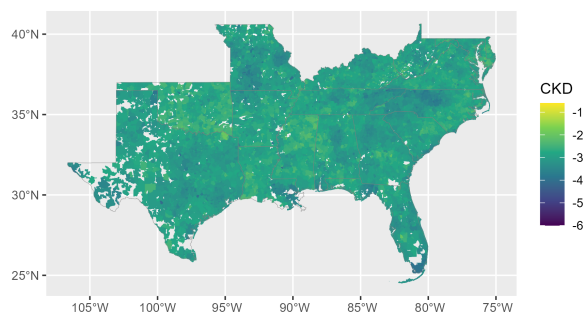
(e) Mean Width of 95% Credible Intervals

ϕ	β_{XZ}	coefficients	MSM	USM	Naive	Spatial+80	Spatial+40
1	1	nonzero	1.42 (0.05)	1.91 (0.07)	0.70 (0.01)	1.03 (0.01)	1.75 (0.01)
1	2	nonzero	1.51 (0.06)	1.85 (0.07)	0.59 (0.00)	0.95 (0.01)	1.70 (0.01)
2	1	nonzero	1.41 (0.05)	1.94 (0.07)	0.74 (0.01)	1.07 (0.01)	1.77 (0.01)
2	2	nonzero	1.50 (0.06)	1.94 (0.07)	0.67 (0.01)	1.07 (0.01)	1.77 (0.01)
1	1	zero	1.28 (0.06)	1.45 (0.07)	0.82 (0.01)	1.23 (0.01)	2.12 (0.02)
1	2	zero	1.46 (0.07)	1.47 (0.07)	0.69 (0.01)	1.11 (0.01)	2.05 (0.02)
2	1	zero	1.26 (0.06)	1.48 (0.07)	0.88 (0.01)	1.30 (0.01)	2.14 (0.02)
2	2	zero	1.42 (0.07)	1.50 (0.07)	0.79 (0.01)	1.29 (0.01)	2.14 (0.02)

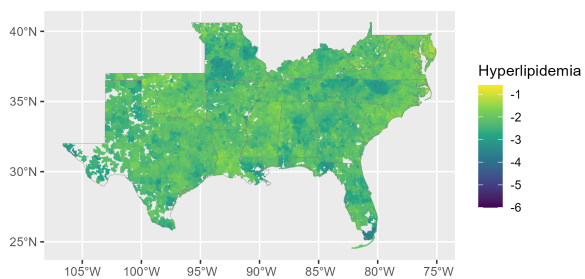
Figure 9: **Maps for health outcomes (log scale):** Five chronic health outcomes in southern states are in (a)-(e). The raw percentages are between 0.003 and 0.55.



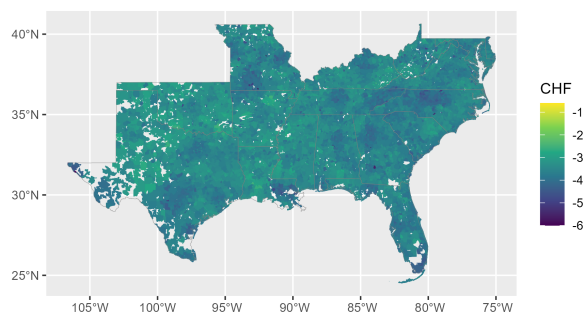
(a) Hypertension



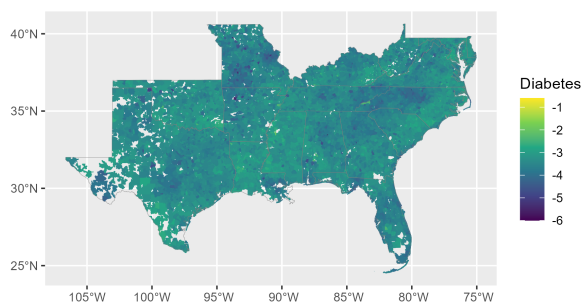
(b) Chronic kidney disease



(c) Hyperlipidemia



(d) Chronic heart failure



(e) Diabetes

Table 5: **MSE and coverage comparison** with different L and K for Setting 2 ($\phi = 1, \beta_{XZ} = 2$), 20 replicates

MSE	nonzero coefficients			zero coefficients		
	L=5	L=10	L=20	L=5	L=10	L=20
K=2	0.06 (0.02)	0.06 (0.02)	0.07 (0.02)	0.02 (0.01)	0.03 (0.01)	0.02 (0.01)
K=5	0.05 (0.01)	0.06 (0.02)	0.06 (0.02)	0.03 (0.01)	0.03 (0.01)	0.02 (0.01)
K=10	0.05 (0.01)	0.05 (0.01)	0.06 (0.02)	0.03 (0.01)	0.03 (0.01)	0.02 (0.01)
Coverage	nonzero coefficients			zero coefficients		
	L=5	L=10	L=20	L=5	L=10	L=20
K=2	0.82 (0.07)	0.87 (0.06)	0.91 (0.05)	0.95 (0.04)	0.98 (0.02)	0.99 (0.00)
K=5	0.99 (0.01)	0.99 (0.01)	0.99 (0.01)	0.99 (0.01)	1 (0.00)	1 (0.00)
K=10	1 (0.00)	1 (0.00)	1 (0.00)	1 (0.00)	1 (0.00)	1 (0.00)

Table 6: **Log scores using 80% training data and 20% test data:** The log scores are the log likelihood of the observed outcomes of the test set, given the predicted mean and standard deviation from the training model.

	L = 5	L = 10
K = 5	-0.911	-0.906
K = 10	-0.910	-0.904